A myelinic channel system for motor-driven organelle transport

Katie J. Chapple[1], Sarah Wirth[1], Yi-Hsin Chen[1], Tabitha R.F Green[1], Ulrike Gerwig[2], Marie Louise Aicher[2], Yeonsu Kim[2], Lina Komarek[1&2], Angus Brown[3], Colin L. Crawford[1], Rebecca Sherrard Smith [1], Luis Pardo-Fernandez[1], Celia M. Kassmann[2], Hauke B. Werner[2], Matthias Kneussel[4], Euan R Brown[5], Sandra Goebbels[2], Klaus-Armin Nave*[2], Julia M. Edgar*[1&2].

1 School of Infection & Immunity, College of Medical Veterinary and Life Sciences, University of Glasgow, Glasgow, G12 8TA

2 Dept of Neurogenetics, Max Planck Institute for Multidisciplinary Sciences

City Campus, Hermann-Rein-Strasse 3, D-37075 Goettingen, Germany

3 School of Life Sciences, University of Nottingham, University Park, Nottingham

NG7 2UH

4 Department of Molecular Neurogenetics, Center for Molecular Neurobiology, ZMNH, University Medical Center Hamburg-Eppendorf, 20251, Hamburg, Germany

5 School of Engineering and Physical Sciences, Institute of Biological Chemistry, Biophysics and Bioengineering, Heriot Watt University, Edinburgh EH14 4AS, UK.

***Correspondence:**

Professor Julia Edgar, School of Infection & Immunity, College of Medical Veterinary and Life Sciences, University of Glasgow, Glasgow, G12 8TA. E-mail: Julia.Edgar@glasgow.ac.uk

Professor Klaus-Armin Nave, Dept of Neurogenetics, Max Planck Institute for Multidisciplinary Sciences, Campus City, Hermann-Rein-Strasse 3, D-37075 Goettingen, Germany. E-mail: Nave@mpinat.mpg.de

Abstract

Myelin sheaths comprise compacted layers of oligodendroglial membrane wrapped spirally around axons. Each sheath, if imagined unwrapped, has a cytoplasm-filled space at its perimeter, linking it to the oligodendrocyte soma via a short process. By electron microscopy (EM), this space, which we term the '*myelinic channel system*' contains microtubules and membranous organelles, but whether these are remnants of development or serve a function is unknown. Performing live imaging of myelinating oligodendrocytes expressing fluorescent reporters, we found that the myelinic channel system serves microtubule-dependent organelle transport. Further, the intra-myelinic movement of peroxisomes was modulated by neuronal electrical activity in these mixed neural cell cultures. Loss of oligodendroglial Kif21b or CNP *in vivo* led to apparent stasis of myelin organelles and secondary axon pathology. This suggests that oligodendrocytes require motor transport in the myelinic channel system to maintain axonal integrity.

Keywords: microtubule-dependent transport; action potential, intra-cellular transport

Introduction

In the nervous system, the unusual size and architecture of neurons with long axons requires an intracellular transport system for moving cargo between the neuronal somata and distant axonal terminals. Axonal transport has been studied in detail since it was first described in the 1960s (Allen et al., 1982; Austin et al., 1966; Brady et al., 1982; Grafstein, 1967; Lasek, 1967; Livett et al., 1968; Lubinska, 1964; Ochs et al., 1967; Weiss and Holland, 1967), including its molecular mechanism involving motor protein transport on microtubular tracts (Brady, 1985; Cason and Holzbaur, 2022; Vale et al., 1985; Vargas et al., 2022; Zahavi and Hoogenraad, 2021). Here we show that a related logistical challenge exists at a much smaller scale with respect to the vital interaction of process-bearing oligodendrocytes and the axons they myelinate. Compacted myelin facilitates the rapid conduction of neuronal electrical impulses, by decreasing the capacitance and increasing the electrical resistance across the myelinated fibre, and confining action potential generation to the nodes of Ranvier (Cohen et al., 2020; Hartline and Colman, 2007). However, in so doing, myelin separates spatially the oligodendrocyte soma from the internodal axon-glial junction (Figure 1A), a 20 nm wide synapse-like gap (Stys, 2011), thought to mediate the exchange of metabolites through monocarboxylate transporters (Fünfschilling et al., 2012; Lee et al., 2012).

In CNS development, each myelin sheath is derived from a lamellipod connected by a narrow cell process to the oligodendrocyte soma. Growth of the prospective sheath involves actin remodelling (reviewed in Brown and Macklin, 2020) at the lamellipod's leading edge (future 'inner tongue'), which advances in a myelin basic protein-(MBP) -dependent fashion around the axon, underneath accumulating numbers of membrane wraps (Nawaz et al., 2015; Snaidero et al., 2014; Zuchero et al., 2015). Simultaneously, the lamellipod grows along the axon's length (Snaidero et al., 2014) in response to calcium signalling in the oligodendrocyte (Iyer et al., 2024), and requiring nucleation of microtubules (Fu et al., 2019). Membrane compaction occurs by an MBP-dependent fusion of

opposing intracellular surfaces (Aggarwal et al., 2011; Harauz et al., 2009), which, combined with tethering of opposing extracellular surfaces of the wrapping lamellipod (García-Mateo et al., 2018), culminates in tightly wrapped concentric layers of membrane. A cytoplasm-filled space remains at the perimeter of the sheath, if imagined unwrapped, suggesting a direct connection to the intracellular contents of the cell soma (Butt and Ransom, 1989) via the cell process (Peters, 1960; Sternberger et al., 1978) (Figure 1A).

This cytoplasm filled space forms the 'inner and outer tongues' at the innermost and outermost longitudinal edges of the spiralled sheath, and arrays of 'paranodal loops' at either lateral end of the sheath (Figure 1A). The latter are tightly tethered to the axon by septate-like junctions (Bhat, 2003). Other cytoplasm-filled spaces in CNS myelin include transient openings of the compacted myelin, associated with secondary myelin growth (Snaidero et al., 2017; Velumian et al., 2011), rare Schmidt-Lanterman incisure-like openings on large fibres (Blakemore, 1969) and other conformations not yet fully defined (Edgar et al., 2021; Weruaga-Prieto et al., 1996). Myelin's cytoplasm-filled spaces are generated and maintained, at least in part, by 2′,3′-cyclic nucleotide 3′-phosphodiesterase (CNP), which limits the membrane 'compacting' function of MBP (Snaidero et al., 2017; Trapp et al., 1988).

When analysed by EM, myelin's cytoplasm-filled spaces, which we term the "myelinic channel system", contain microtubules, endoplasmic reticulum, vesicle-like structures, multivesicular bodies, peroxisomes and Golgi outposts (Edgar and Griffiths, 2013; Frühbeis et al., 2020; Nakamura et al., 2021; Richert et al., 2014; Stassart et al., 2018). Since all these compartments have been implicated in developmental myelination, it remains unknown whether they exist as remnants of myelinogenesis, captured in the mature sheath, or whether they play a functional role in mature white matter tracts. We previously speculated that in the adult nervous system, the myelinic channel system, provides a route for soluble oligodendroglial metabolites to reach the glial-axonal junction (Edgar et al., 2009; Meschkat et al., 2020; Nave, 2010a; Saab et al., 2013). Furthermore, since active transport processes

can be visualised in cytosolic spaces of flattened myelin-like sheets in oligodendrocyte monolayer cultures (Ainger et al., 1993; Carson et al., 1997; Kachar et al., 1986; Song et al., 2003), we additionally hypothesized that myelinic channels might serve as a route for the movement of membranous cargo to the glial-axonal junction, analogous to axonal transport to synaptic terminals.

Here we demonstrate microtubule-dependent organelle transport in established myelin sheaths and show that ablation from oligodendrocytes of kinesin 21B (Kif21b), a processive motor and modulator of microtubule dynamics (Ghiretti et al., 2016; Muhia et al., 2016; van Riel et al., 2017), leads to late onset secondary axon degeneration *in vivo*. This coincides with reduced levels of monocarboxylate transporter 1 (MCT1) in biochemically enriched myelin. Consistent with this, CNP-deficient mice, that lack myelinic channel integrity (Snaidero et al., 2017) and exhibit axonal degeneration (Edgar et al., 2009; Lappe-Siefke et al., 2003), and similarly in aged mice with structural myelin defects, the level of MCT1 in myelin is markedly diminished. As MCT1 resides at the glial-axonal junction and is thought to mediate the transfer of monocarboxylates between oligodendrocytes and axons (Fünfschilling et al., 2012; Lee et al., 2012), our data suggest myelinic transport is vital for oligodendrocyte-mediated axon support

Results

The myelinic channel system and its organelle content.

The myelinic channel system (yellow in Figure 1A) includes the outer and inner tongues and the paranodal loops of myelin. To define a putative transport infrastructure, we used transmission electron microscopy (EM) of adult mouse optic nerve cross sections. As reported previously (reviewed in Edgar and Griffiths, 2013), some inner tongues of myelin contained microtubules (Figure 1B; usually 1-2 per tongue), which were also observed in outer tongues and paranodal loops (**Supplementary Figure 1A and B)**. Multivesicular bodies (Figure 1C and see Frühbeis et al., 2020) and single membrane structures resembling peroxisomes (Figure 1D) could be found in inner and outer tongues and paranodal loops, and very rarely, in cytosolic pockets of otherwise compact myelin (**Supplementary Figure 1C**). Some membrane-bound structures in inner tongues (Figure 1E) and paranodal loops had a pale core similar to the axoplasm, compatible with the hypothesis these are invading axonal sprouts (Steyer et al., 2023). Of the 2348 optic nerve axon cross-sections examined, 0.82 % (+/- 0.45 SD; n = 4 optic nerves of 12-month-old mice) of inner tongue processes contained structures resembling peroxisomes or multi-vesicular bodies. Based on (i) EM tissue sections being ~50 nm thick, (ii) the average optic nerve myelin sheath length being ~76 µm (Young et al., 2013) and the assumption that (iii) organelles are distributed randomly and (iv) spherical in shape, being ~0.3 µm in diameter (Figure 1C and D), our data suggest that the inner tongue of each optic nerve myelin sheath contains ~2 such organelles (as paranodal loops are encountered only infrequently in EM images, we were unable to independently determine their organelle content using this method). In addition to myelin organelles, we observed invaginations of glial membrane into the axon (Figure 1F and **Supplementary Figure 1D-F)**, similar to previous reports in peripheral nerves (Spencer and Thomas, 1974). Very rarely, the myelin membrane even formed fusion-like profiles with the peri-axonal space (**Supplementary Figure 1G**), suggesting direct exchange of materials between the two compartments.

As glutamate, which is released from electrically active axons (Micu et al., 2016), enhances the release of exosomes from oligodendrocytes *in vitro* (Frühbeis et al., 2020), we next asked if axonal electrical activity influences the localisation of organelles to myelin's inner tongue, alongside the periaxonal space (Figure 1A). To address this, we used an *ex vivo* optic nerve preparation in which we could precisely control action potential firing using stimulating and recording suction electrodes (**Supplementary figure 1H**), as described (Stys et al., 1991). One of each pair of adult mouse optic nerves was unstimulated while the contralateral nerve was stimulated to fire constitutively at 7 or 50 Hz for 20 minutes. By EM of nerve cross section, the stimulated nerve had more inner tongues with organelles (average 0.65% +/- 0.28 SD: ~1.7 organelles per sheath) compared to the unstimulated contralateral nerve (average 0.32 % of fibres +/- 0.34 SD; ~0.8 organelles per sheath), although with 5 nerve pairs analysed, the differences were not yet significant (**Supplementary Figure 1I-K**). While organelle numbers could also decrease due to fusion, these data led us to hypothesize that organelle transport in the inner tongue might be modulated by axonal electrical activity.

Next, we focussed on peroxisomes, using a transgenic mouse in which oligodendroglial peroxisomes are labelled with the photoconvertible fluorescent protein mEOS2 (Richert et al., 2014). To demarcate the myelinic channel system, we additionally labelled a proportion of oligodendrocytes with a transgenically-expressed, tamoxifen-inducible fluorescent protein (Edgar et al., 2021), td-tomato. In longitudinal sections of optic nerve, mEOS2-labelled peroxisomes were observed in the oligodendrocyte soma; at paranodes, as indicated by axonal expression of Caspr1; and in internodal myelin (Figure 1G). This was confirmed in spinal cord (**Supplementary Figure 1L**). However, in the densely packed white matter it was difficult to resolve individual myelin sheaths, even with sparse labelling of oligodendrocytes. Therefore, for subsequent observations, we used a murine spinal cord-derived myelin-forming coculture of neurons and glia (Bijland et al., 2019). Here, as *in vivo*,

oligodendrocyte peroxisomes were observed in td-tomato rendered somata, processes, and sheaths (Figure 1H and **Supplementary Figure 1M**), including inner and outer tongues (Figure 1I and J) and 48.2% (+/- 7.4 SD) of paranodes examined (Figure 1K and 1H-K; **Supplementary Figure 1M**).

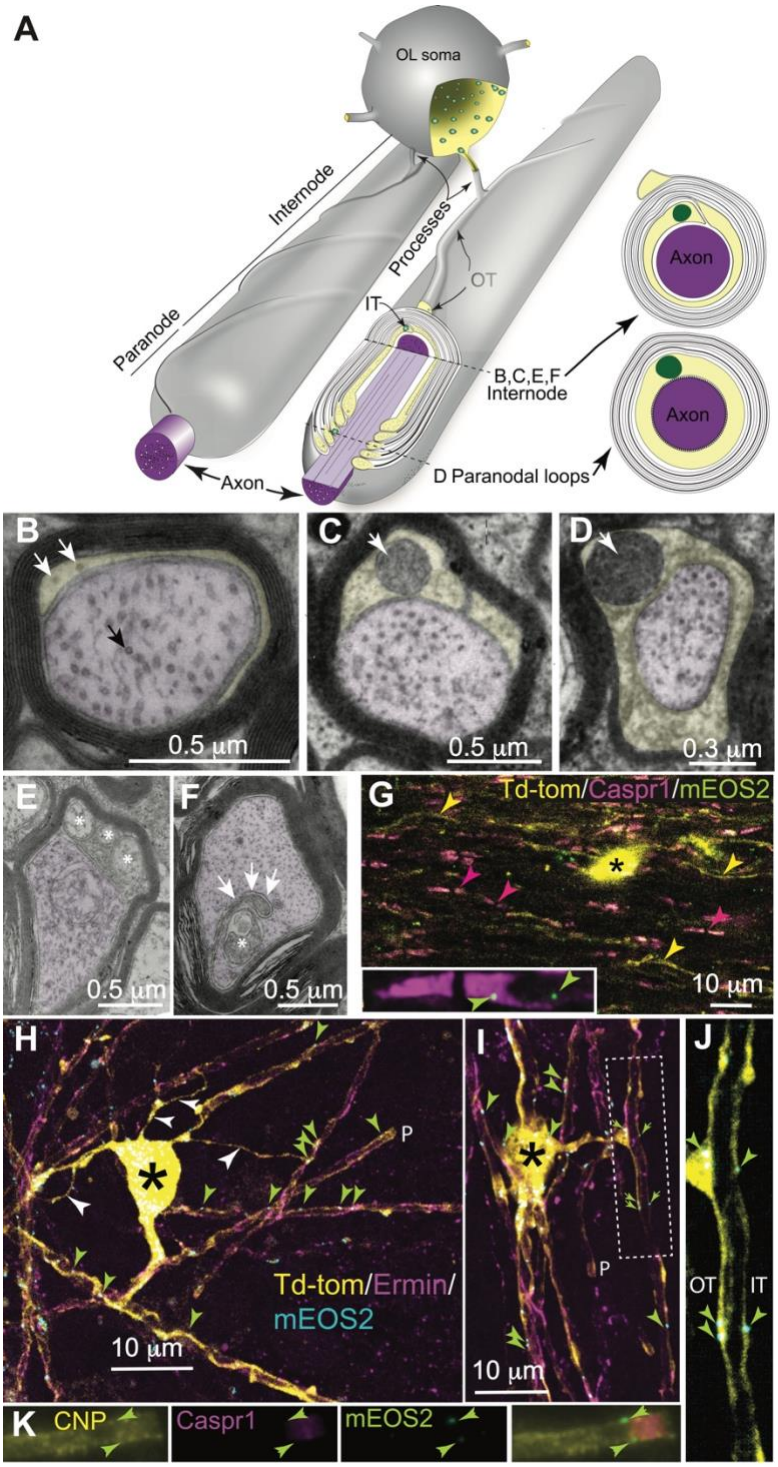

Figure 1. Microtubules and membranous organelles in the myelinic channel system.

A. Schematic depiction of an oligodendrocyte soma (OL) and two myelin sheaths. Cytoplasm (yellow) fills the myelinic channel system including inner and outer tongues (IT, OT) that entwine the myelin sheath on its inner and outer surfaces, respectively, and the paranodal loops that are tethered to the axon at the paranode. Myelin organelles and vesicular structures are represented in green. Two dashed lines depict approximately where the cross sections in the corresponding EM images are located.

B-F. Micrographs of myelinated axon cross-sections including the inner tongue (B, C and E), a paranodal loop (D) and an invagination of myelin membrane into the axon (F). In B, the black arrow indicates an axonal microtubule, and the white arrows indicate similar structures in myelin's inner tongue. In C, a multivesicular body occupies the inner tongue and in D, a dense organelle resembling a peroxisome, resides in a paranodal loop. In E, three membrane-bound structures reside in myelin's inner tongue. These have a pale core (asterisks), similar to the axoplasm, suggesting they are axonal sprouts. In F, an invagination of the glial cell membrane (arrows) surrounds an abnormal-appearing axonal organelle (asterisk), as shown previously (Spencer and Thomas, 1974).

G. Maximum intensity projection (MIP) from a confocal z-stack of a longitudinal section of the optic

nerve in which oligodendrocytes and myelin are labelled with td-tomato (pseudo coloured yellow), oligodendrocyte peroxisomes are labelled with mEOS2 and paranodes are immunostained with anti-Caspr1, which is located on the axon. Peroxisomes are observed in somata (in this case, obscured by td-tomato) and myelin sheaths (yellow arrows), including paranodes (magenta arrows). Some peroxisomes reside in non-td-tomato rendered-cells. Inset: two Caspr1 stained paranodes separated by a node of Ranvier. By inference, the two peroxisomes are located in paranodal and internodal myelin, respectively.

H. MIP of an oligodendrocyte *in vitro* labelled with td-tomato and anti-Ermin, a cytoskeletal molecule that first appears during late myelination stages (Brockschnieder et al., 2006). The soma is marked with an asterisk and a paranode with P. mEOS2-labelled peroxisomes can be observed in the processes (white arrowheads) and myelin sheaths (green arrows).

I. MIP of a second td-tomato-rendered oligodendrocyte showing peroxisomes (green arrows) in myelin sheaths including in the triangular shaped thickening at the junction of the process and the sheath.

J. High magnification view of sheath delineated by dotted line in I. Peroxisomes reside in both outer and inner tongues (OT and IT).

K. Paranodal region from a cell labelled with anti-CNP (myelin) and anti-Caspr1. Two mEOS2-labelled peroxisomes are visible; by inference, the lower one is located just inside the paranodal region, marked by Caspr1, and the other at the juxtaparanode, between the internode and the paranode.

Myelinic organelle transport is microtubule dependent.

The optic nerve stimulation experiment suggests that myelin organelles are motile. To explore this further, we used live imaging of mEOS2+ oligodendrocyte peroxisomes in mixed neuron-glial co-cultures in which td-tomato-labelled oligodendrocytes wrap axons with an appropriately thick compact myelin sheaths (Edgar et al., 2021; Thomson et al., 2008). As in other mammalian cell types (Wali et al., 2016) most myelin peroxisomes were apparently stationery or underwent only short-distance, Brownian-like motion. However, within a 10-minute imaging window, 16.2% (± 4.07 SD) of myelin peroxisomes exhibited movement (traversing distances ≧ 3 μm; Figure 2A and B and covering distances up to ~70 μm. Travel was punctuated by periods of stasis (Figure 2A), such that the overall velocity over 10 minutes was approximately 10× less than when motile; the latter being 0.18 μm/sec (± 0.02 SD), on average. Some peroxisomes travelled predominantly in one direction (Figure 2A-C), while others reversed direction (indicated by circles in **Supplementary Figure 2**) and/or crossed paths with another (indicated by orange crosses in **Supplementary Figure 2**). Often, peroxisomes in the outer tongue (where it could be determined definitively) travelled towards the paranode (Figure 2B and C; **Supplementary Videos 1 and 2**). In **Supplementary Video 3** a peroxisome travels to the paranodal loops of myelin via the presumptive outer tongue, traverses 4

paranodal loops and travels back in the direction of the cell body via the presumptive inner tongue.

In other eukaryotic cell types, peroxisomes are transported on microtubules (Rapp et al., 1996 and reviewed in Covill-Cooke et al., 2021). To determine if this is also true in the myelinic channel system, we treated myelinating cell cultures with nocodazole, which interferes with the polymerization of microtubules (Kesarwani et al., 2020). As axons also contain microtubules, we aimed to minimise confounding effects on myelinic transport (caused by axon dysfunction) by using a concentration and incubation time that did not markedly alter the microtubule network in neurons. In these cell dense cultures, 3-hours in 20 μM nocodazole led only to minor alterations in anti-β-tubulin 3 staining (**Supplementary Figure 3**), indicating that neuronal microtubules were only partially disrupted over this time period. Furthermore, detyrosinated tubulin, a non-cell type specific marker of stable microtubules, appeared similar to controls (**Supplementary Figure 3**). Using this protocol, nocodazole caused a significant reduction in the percentage of motile myelinic peroxisomes (Figure 2D) without altering their velocity during motile phases (Figure 2E). Nonetheless, the average velocity of individual organelles (including motile and stationary phases) within the 10-minute imaging period, shifted towards slower speeds (Figure 2F). Consequently, the maximum distance travelled by a single peroxisome in this experimental series was reduced from 55.0 μm in controls to 23.8 μm in nocodazole-treated cells, likely reflecting the drug's perturbation of microtubular tracks. Indeed, in DMSO-treated control cultures, β–tubulin 4 (which is specific in the CNS to oligodendroglia) stained continuous structures within myelinic channels in 94 % (+/- 2.0 SD) of td-tomato positive cells (Figure 2G and **Supplementary Figure 3**; *n* = 33 cells; 2 independent cell cultures), but in only 45 % (+/- 7.0 SD) of td-tomato positive cells after nocodazole-treatment (Figure 2H and **Supplementary Figure 3**; *n* = 17 cells; 2 independent cell cultures). Notably, in both control and nocodazole-treated cultures, the amount of polymerised β-tubulin 4 varied considerably from sheath to sheath and from cell to cell. In summary, myelinic channels enable an active, microtubule-dependent transport of peroxisomes, and presumably other membrane-bound cargo.

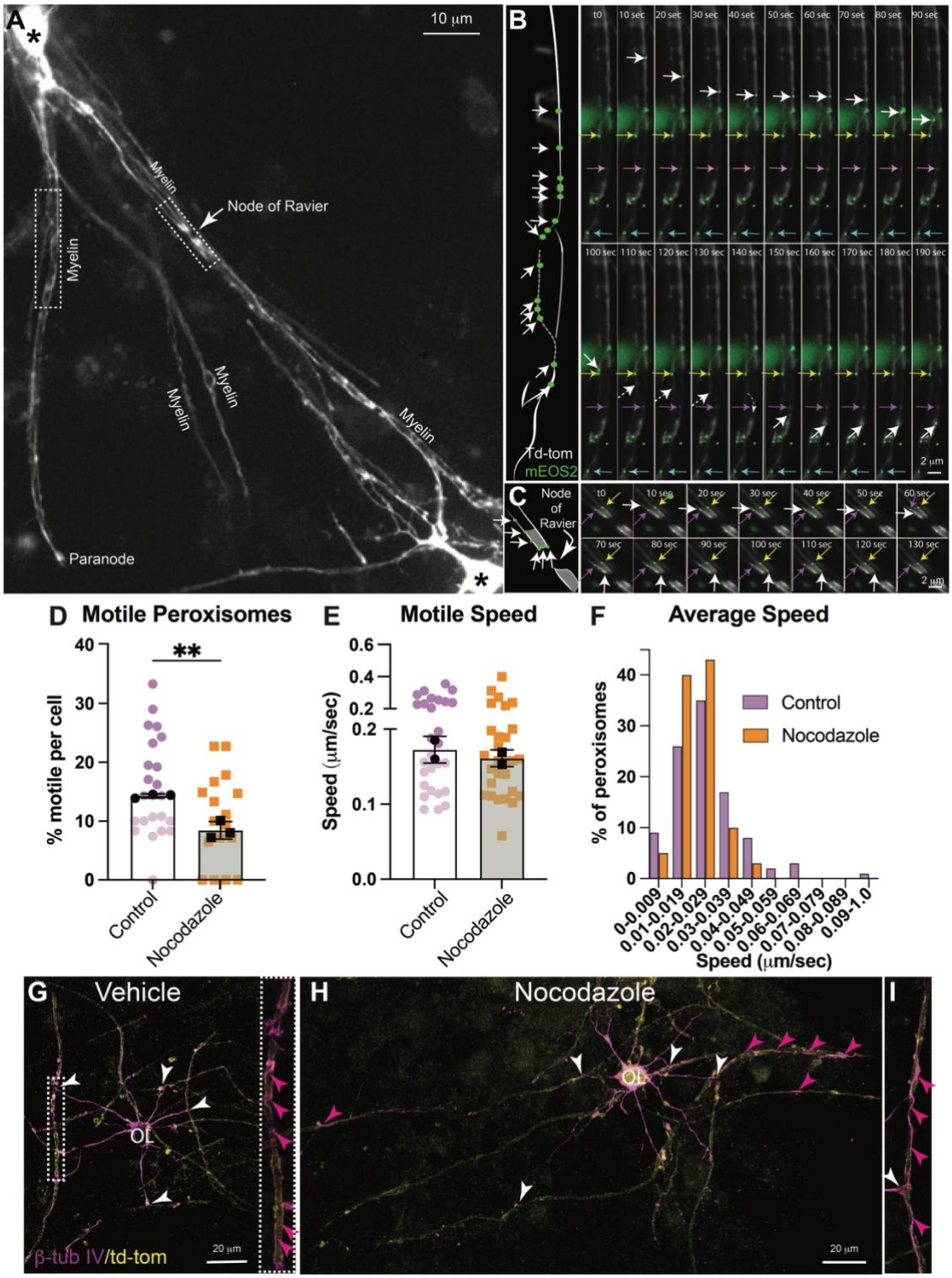

Figure 2. Myelinic peroxisome transport is microtubule-dependent.

A. Overview of two td-tomato rendered oligodendrocytes (somata are labelled with asterisks) from which the timelapse images in B and C were acquired.

B and C. The schematics on the left illustrate the totality of the movement of a single myelin peroxisome in each of the timelapse movies depicted on the right. Lines represent cytoplasm-filled spaces within (solid lines) and outside (dashed lines) the focal plane. In B, the timelapse images show

a motile peroxisome (white arrows) move down the presumptive outer tongue towards the paranodal loops (see overview), slowing or stalling at 30, 110 and 160 sec time points. At 140 secs, the organelle moves out of the focal plane and the path (small white arrow) is inferred from the movie. Most peroxisomes (coloured arrows) were stationery. In C, paranodal regions of adjacent sheaths, are separated by a node of Ranvier (see overview). A motile peroxisome (white arrow) moves down the outer tongue process (determined from the relationship to the node of Ranvier) and traverses the presumptive paranodal loop nearest the node of Ranvier, before moving out of the focal plane. Other peroxisomes (coloured arrows) were stationery.

D. Nocodazole (20 μM, 3-hour incubation) reduced the percentage of myelin peroxisomes that were motile during the 10-minute period. Coloured symbols represent individual oligodendrocytes, black symbols represent experimental medians; bars indicate mean of the median values +/- SD. An unpaired Student's *t* test was used to compare the means. ** $p < 0.01$.

E. Nocodazole did not alter the velocity of individual myelin peroxisomes when motile. Coloured symbols each represent one motile peroxisome and black symbols represent experimental medians; bars indicate the mean of the median values +/- SD.

F. Nocodazole caused a shift to slower average velocities, reflecting motile and stationary phases, of individual peroxisomes during the 10-minute imaging period, likely reflecting a reduction in available transport tracks.

G-I. β−tubulin IV staining of td-tomato labelled oligodendrocytes, following extraction of free tubulins, treated with DMSO (vehicle; G) or nocodazole (20 μM, 3 hours; H and I). White arrows indicate where processes from the oligodendrocyte attach to the myelin sheath and magenta arrows indicate regions of continuous β−tubulin IV staining. The sheath delineated by a white rectangle in D is shown at higher magnification in the inset. The sheath in I is from a different cell from that in H.

Myelin microtubules harbour post-translational modifications

Our data suggested that some myelin microtubules are more resistant to nocodazole than others, suggesting that myelin contains mixed populations of "dynamic" and "stable" microtubules (Jansen et al., 2023). Microtubule stability is encoded in post-translational modifications of tubulins, and the presence of differentially modified tubulins is crucial in the assembly, disassembly and rearrangement of the microtubule cytoskeleton (Borys et al., 2020; Janke and Bulinski, 2011). Recently, genetic sensors were developed that identify tyrosinated microtubules (AlaY1; (Kesarwani et al., 2020), which are generally considered to be rather labile; or stable microtubules (StableMARK; Jansen et al., 2023), which are generally acetylated and/or detyrosinated. We observed both genetic sensors in oligodendrocyte cell bodies, processes, and myelin sheaths (Figure 3A and B). However, as StableMARK can by itself stabilise microtubules, and as AlaY1 also labels free tubulins, we next used antibody staining, following extraction of free tubulins (Jansen et al., 2023), to identify post-translational modifications (PTMs) on microtubule polymers. Anti-tyrosinated tubulin partially labelled one or more myelin sheaths in 83% of all td-tomato positive oligodendrocytes (n = 12 cells;

3 independent cell cultures) (Figure 3A and B). Anti-detyrosinated tubulin was not observed in myelin sheaths (Figure 3C). Acetylated tubulin was observed in some sheaths (Figure 3D, E), as reported previously (Kusch et al., 2017; Werner et al., 2007). Because the antibodies to tyrosinated and acetylated tubulin are raised in the same species, we were unable to determine if different PTMs co-exist in the same sheaths.

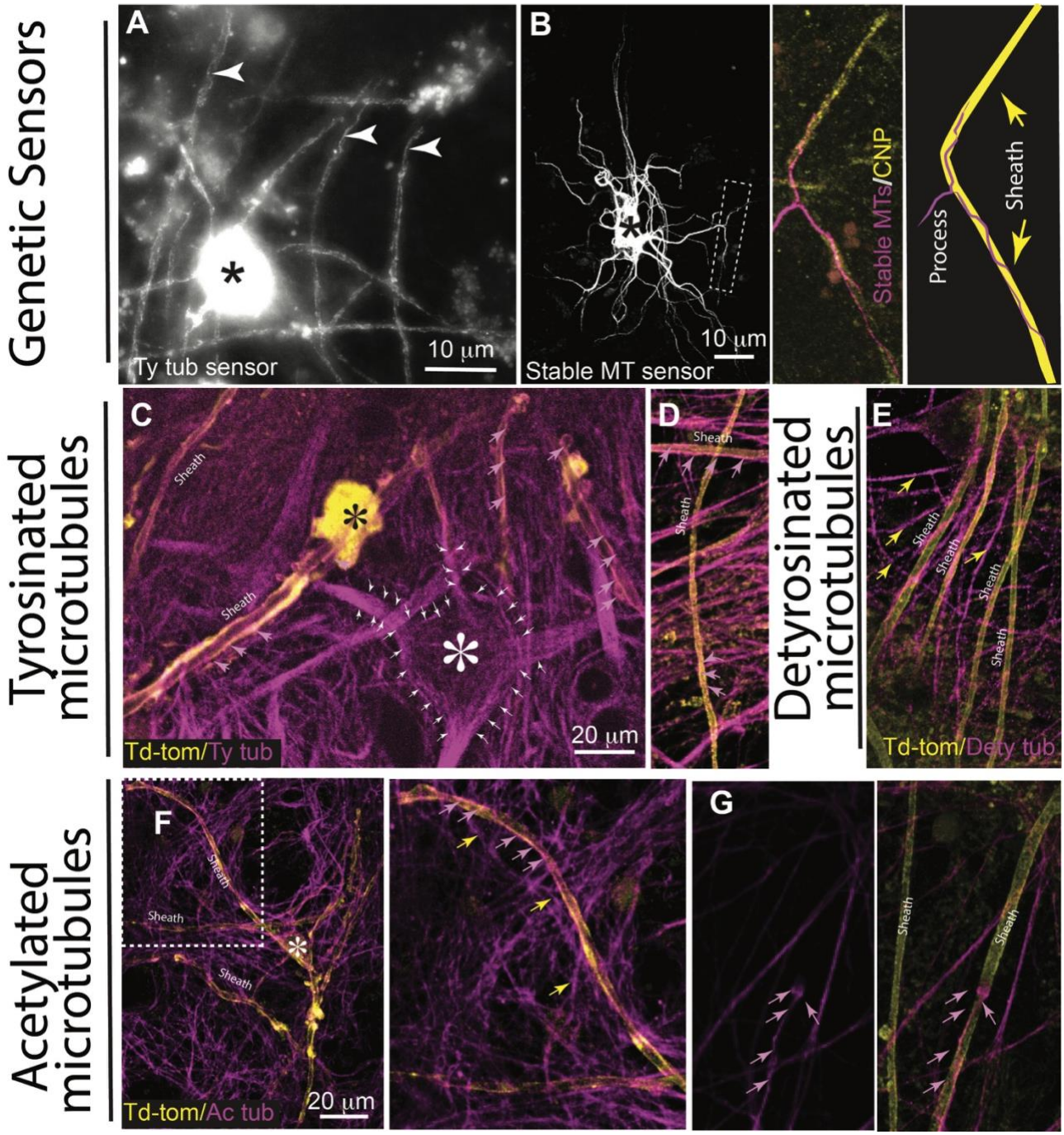

Figure 3. Microtubules in myelinic channels harbour various post-translational modifications.

A and **B**. Nine hours after oligodendrocyte transfection, genetic sensors labelling tyrosinated tubulins (Ty tub) (A) and stable microtubules (stable MTs) (B) in myelin, were visible. In A, arrowheads point

to continuous-appearing structures suggesting they are microtubule polymers in myelinic channels. In B, the cell body labelling is saturated, and processes are intensely labelled. A higher magnification view of an associated myelin sheath (delineated by the broken line), is seen on the right, stained with anti-CNP and illustrated for clarity in the schematic. The abnormal appearance of the somata and processes is likely because StableMARK itself stabilises microtubules.

C-F. Following extraction of free tubulins, immunocytochemistry was used to identify PTMs on myelin microtubules. Anti-tyrosinated tubulin labelled some myelin sheaths (magenta arrows) of td-tomato labelled cells, and the cell bodies (asterisk) and processes of other cell types (C). In general, anti-tyrosinated tubulin only partially labelled sheaths (magenta arrows; D). Anti-detyrosinated tubulin did not colocalise with td-tomato positive sheaths but labelled other cell processes (yellow arrows). Where magenta and yellow coincide, the tubulin stain does not follow the contours of the sheath, suggesting it is the processes of overlapping cells (E). Anti-acetylated tubulin labelled a few myelin sheaths (magenta arrows) although it was prevalent in other cellular processes (yellow arrows). The oligodendrocyte soma is labelled with an asterisk in the overview image on the left (F). Anti-acetlylated tubulin only partially labelled sheaths (G).

Together these data demonstrate tubular tracks within the myelinic channel system are required for active translocation of organelles. Interrogation of our databases of purified myelin proteins, identified by label-free mass spectrometry (Gargareta et al., 2022; Jahn et al., 2020) provided further evidence for the presence in myelin of tubulins, microtubule binding proteins, tubulin modifiers, molecular motors and peroxisomal markers, such as catalase (**Supplementary Table 1**).

Modulators of neuronal activity influence the motility of myelin peroxisomes

Myelin-associated peroxisomes are essential for the long-term integrity of axons, particularly faster spiking axons, which are most vulnerable to peroxisomal defects (Kassmann et al., 2007) Axonal spiking activity and glutamatergic signalling also trigger neuroprotective exosome release and oligodendroglial metabolic support (Frühbeis et al., 2020; Saab et al., 2016); the latter as an oligodendroglial calcium response (Looser et al., 2022) that is seen also during developmental myelination (Baraban et al., 2018; Krasnow et al., 2018). As a simple cellular model to examine the response of myelin-associated peroxisomes to changes in neuronal firing, we used myelinating cell cultures, in which neuronal electrical activity and neuronal energy consumption can be enhanced with the GABA receptor blocker picrotoxin (PTX; 100 μM) or diminished with tetrodotoxin (TTX; 1 μM) (Figure 4A and B).

Live imaging of oligodendrocyte processes over a 10-minute timeframe (beginning 5-minutes post drug application) showed that modulating neuronal activity had no effect on retrograde or anterograde transport of peroxisomes between the myelin sheath and the oligodendrocyte soma (**Supplementary Figure 4A, Supplementary Video 4**). This is in agreement with our observation that peroxisomes entered the 'myelin sheath' even when formed on inert fibres (Figure 4C). Nonetheless, in the presence of neurons, myelin-associated peroxisomes responded to PTX or TTX by becoming more or less motile, respectively (Figure 4D), demonstrating that neuronal activity influences myelinic transport processes locally. Despite this, the number of peroxisomes at paranodes did not change in response to changes in neuronal activity, at least in the short term (**Supplementary Figure 4B**).

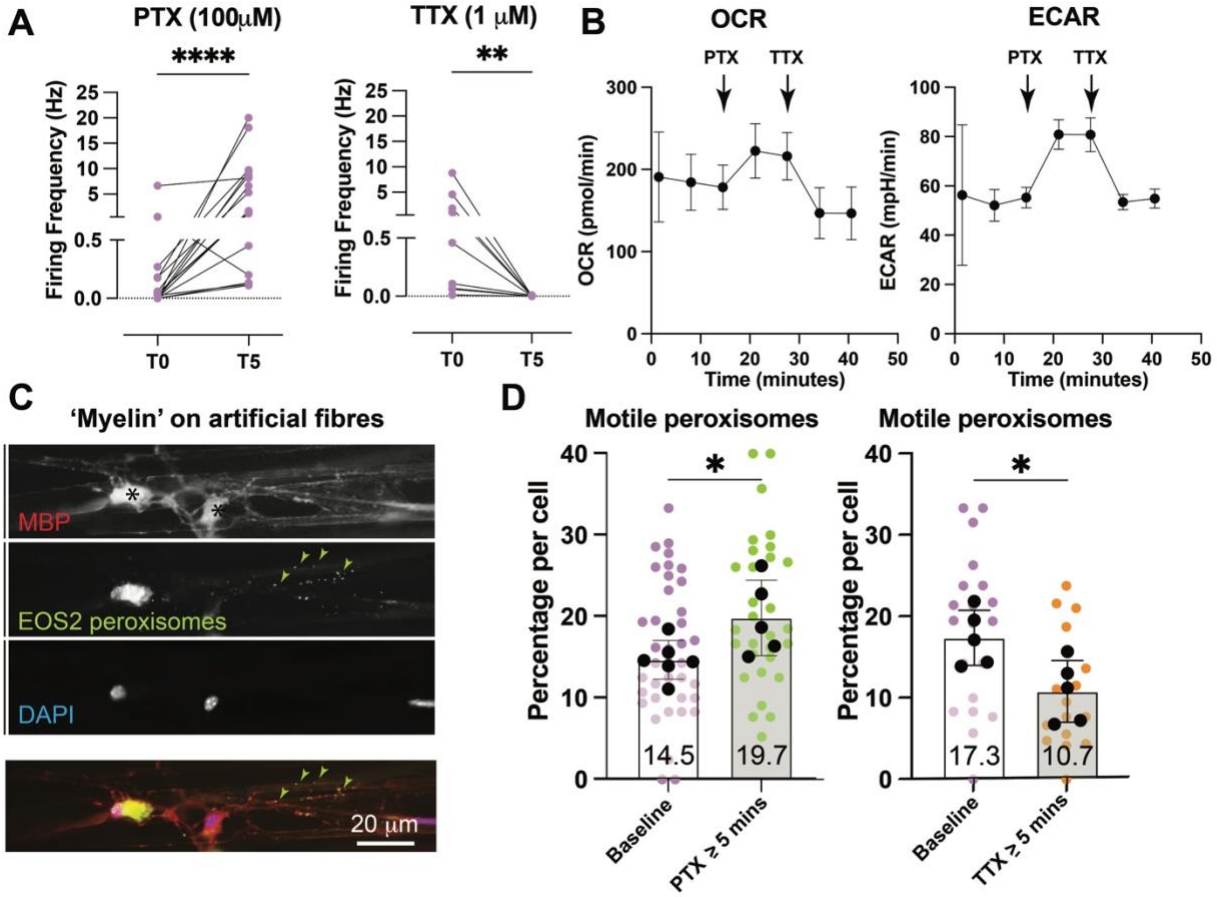

Figure 4. Neuronal activity locally modulates the movement of myelin peroxisomes.

A. In myelinating cell cultures, PTX or TTX enhance or block neuronal activity, respectively. Graphs show firing frequency of individual neurons recorded in patch clamp at baseline (T0) and 5 minutes (T5) after the application of drug. A paired Student's t test was used to compare

pre- and post-drug values. Results are from 9 and 5 independent cell cultures, respectively **** p = <0.0001; ** p = <0.01.

B. In neuron-enriched cultures, oxygen consumption rate (OCR) and extracellular acidification rate (ECR) changed in response to PTX or TTX indicating a general increase and decrease, respectively, in energy consumption. Symbols represent the mean of 3 independent experiments. Error bars represent SD.

C. Widefield epifluorescence micrograph of peroxisomes in the MBP positive myelin-like structures formed on inert fibers, demonstrating that neuronal activity is not necessary for peroxisomes to enter the sheath during myelinogenesis.

D. Graphs showing the proportion of myelin peroxisomes per cell that are motile during a 10-minute imaging period. Coloured dots represent individual cells and black dots represent experimental medians. Bars represent mean of experimental medians +/- SD. PTX or TTX significantly increased or decreased, respectively, the percentage of myelin peroxisomes that were motile during a 10-minute imaging period. An unpaired Student's t test was used to compare pre- and post-drug values between the median values of the independent experiments. Results are from 5 or 6 independent cell cultures. *p = <0.05.

Deleting Kif21b from oligodendrocytes leads to secondary axon loss.

In the CNS, β–tubulin 4 is specific to oligodendrocytes and localized to the somata, processes and myelin (Edgar et al., 2021; Terada et al., 2005 and Figure 3 this manuscript), leading us to hypothesize that β–tubulin 4 could play a role in cargo transport, sheath formation and axon maintenance. However, targeting the *Tubb4* gene selectively in oligodendrocytes in *Tubb4*$^{flox/flox}$::*Cnp1*$^{+/Cre}$ mice did not lead to overt changes in myelinated CNS fibres, even at 14 months of age, except that the g-ratio tended to be slightly higher than in controls (**Supplementary Figure 5**). Thus, *Tubb4* function is likely compensated for by other β-tubulins.

Next, we turned to a motor protein, kinesin 21B (Kif21b) that we identified as a putative candidate for a function in the myelinic channel system because polymorphisms in *KIF21B* have been associated with increased susceptibility to multiple sclerosis (MS). Moreover, *KIF21B* is upregulated ~10 fold in MS white matter irrespective of genotype (Goris et al., 2010; Kreft et al., 2014) and expression of *Kif21b* is differentially regulated in different populations of mature oligodendrocytes in spinal cord of experimental autoimmune encephalomyelitis (Zheng et al., 2023). Kif21b is both a

plus end directed progressive motor protein and a modulator of microtubule dynamics (Ghiretti et al., 2016; Hooikaas et al., 2020; Muhia et al., 2016; van Riel et al., 2017) that in neurons, is enriched in dendrites and growth cones at neurite tips (Labonté et al., 2014; Marszalek et al., 1999). To determine if Kif21b is expressed in oligodendrocytes in the optic nerve, we compared by western blotting, optic nerve lysates from *Kif21b* conditional knockout mice (*Cnp1*$^{Cre/+}$::*Kif21b*$^{flox/flox}$) with two controls (*Cnp1*$^{+/+}$::*Kif21b*$^{flox/flox}$ and *Cnp1*$^{+/Cre}$::*Kif21b*$^{+/flox\ or\ +/+}$). Whilst *Cnp1*^{Cre} can recombine ectopically (Genoud et al., 2002), retinal ganglion cells (whose axons traverse the optic nerve) do not recombine, and in the optic nerve, all recombined cells are oligodendrocytes (Saab et al., 2016; Späte et al., 2024). Kif21b was not detected by western blotting of whole optic nerve lysates from *Kif21b* conditional knockout mice but was readily detectable in control optic nerves (Figure 5A), demonstrating in this white matter tract, Kif21b is predominantly expressed by *Cnp1*-expressing oligodendrocytes.

To determine if ablating Kif21b from oligodendrocytes had consequences for the myelinated axon, we examined optic nerve cross sections by EM (Figure 5B-D). Across all genotypes, most myelinated axons appeared morphologically normal at 1 year of age (Figure 5B(i); 5C (i,iii) and 5D (i, ii)). However, in *Kif21b* conditional knockout mice, inner tongues often appeared distended and contained membranous material (Figure 5D (iii, iv)) and occasionally healthy-appearing axons contained mitochondria lacking normal-appearing cristae (Figure 5D iv). Accumulations of axonal organelles (magenta arrows, Figure 5D vi), indicative of axonal transport stasis (Edgar et al., 2004), were observed in *Kif21b* conditional knockout mice from 6 months of age (Figure 5E). Importantly, these pathological features were “lost” at age 9-12 months, but the decline in absolute axon number suggested these pathologically affected axons have degenerated with age (Figure 5E).

While similar pathological axonal changes were seen occasionally also in heterozygous *Cnp1*$^{+/Cre}$ controls at 9-12 months of age, there was no comparable loss of optic nerve axons suggesting that

Kif21b-dependent transport in oligodendrocytes (and/or microtubule destabilisation) is required for long-term axonal integrity.

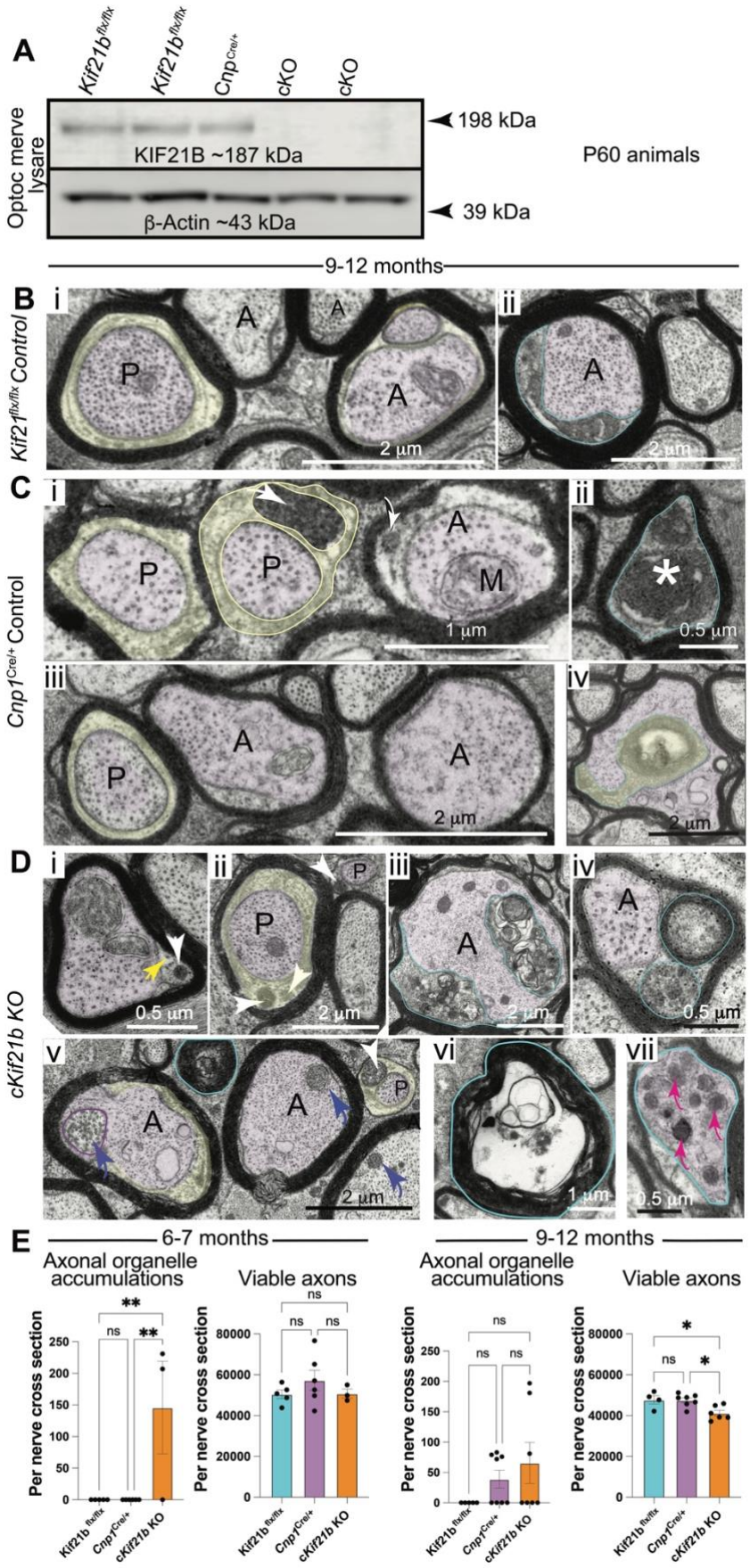

Figure 5. Depletion of Kif21b from oligodendrocytes leads to secondary axon loss.

A. In the optic nerve, a pure white matter tract lacking neuronal cell bodies and dendrites, *Cnp1*Cre-dependent deletion of *Kif21b* led to depletion of Kif21b in whole nerve lysate, demonstrating this motor protein is expressed in oligodendrocytes

B. Electron micrographs of optic nerve axons from 9-12 month *Cnp1*$^{+/+}$::*Kif21b*$^{flx/flx}$ controls. Note the exceptional finding of periaxonal electron dense material (blue outline, Bii).

C. In *Cnp1*$^{Cre/+}$ control optic nerves, myelinated axons appeared largely normal. Periaxonal electron dense organelles in Ci (white arrows) are also seen in WT mice (Figure 1). Rarely, axons appeared electron dense and degenerating (asterisk Cii) or myelinic channels were abnormally extended (blue outline in Civ).

D. In *Kif21b* conditional KO nerve (c*Kif21b* KO), most myelinated axons appeared morphologically normal (Di and ii). Myelinic organelles were observed in myelin's inner tongue (Di) and paranodal loops (Dii) as in WT (Figure 1). In Di, the yellow arrow points to a microtubule. However, myelinic channels were occasionally locally enlarged, impinging on the axon (delineated in blue in Diii). Redundant myelin and/or abnormal electron dense material were observed in some swollen inner tongues (delineated in blue in Div). Extracellular myelin whorls (blue

outlines in Dv and vi) were not more frequent than in controls. Rarely, axons contained abnormal-appearing mitochondria (blue arrow on the left in Dv in comparison to the two mitochondria indicated by blue arrows on the right). Axonal organelle accumulations were also a feature of mutant mice (magenta arrows in Dvii.)

E. Quantitation of axonal organelle accumulations and total axon numbers in *Kif21b* cKO optic nerves and controls at age 6-7 (left) and 9-12 months (right). Data were analysed by one-way ANOVA followed by Tukey's multiple comparisons test. * $p < 0.05$; ** $p < 0.01$. A: axon; P: paranode.

A role for CNP1 and KIF21 in maintaining monocarboxylate transporter levels

We hypothesized that axonal integrity is impaired when metabolic support by oligodendrocytes is compromised. Transport processes in myelinic channels could contribute to overall myelin protein turnover, including that of MCT1 at the glial-axon junction. To determine if oligodendroglial Kif21b depletion impacts specific protein levels in myelin, we performed western blotting of spinal cord myelin from mice at postnatal day 60 (P60) and 1 year. As expected, Kif21b itself was strongly reduced in purified myelin from *Kif21b* conditional mutants (Figure 6A), and to a lesser degree in total spinal cord homogenate containing both white and grey matter (**Supplementary Figure 7**). However, the *Cnp1*^{Cre} knock-in allele (resulting in reduced *Cnp1* gene dosage) was likely to contribute to these effects as CNP acts as a strut that maintains the integrity of myelinic channels (Snaidero et al., 2017) and *Cnp1* heterozygosity leads to myelin dysfunction at advanced age (Hagemeyer et al., 2012). Indeed, in myelin from 1 year old *Cnp1*$^{+/Cre}$ littermate controls, Kif21b levels became remarkably variable (Figure 6A). For comparison, myelin oligodendrocyte glycoprotein (MOG), a transmembrane protein on the outer myelin layer, was unaltered in *Kif21b* conditional mutants compared to either control. In contrast, levels of MCT1, which is required at the glial-axonal junction for the transfer of pyruvate/lactate to the periaxonal space (Fünfschilling et al., 2012; Lee et al., 2012) were significantly reduced in 1 year old mutants, but not yet in their P60 counterparts (Figure 6A). Indeed, MCT1 was also reduced in 1 year old *Cnp1*$^{+/Cre}$ controls, confirming that both Kif21b and CNP are required for maintaining normal MCT1 levels at the glial-axon junction. Importantly, there was no significant change in the levels of β–tubulin 4 in purified

myelin from *Kif21b* conditional mutants, suggesting there was no lack of tubular tracks. We thus hypothesize that the loss of myelinic channel integrity (with reduced CNP1 and absence of oligodendroglial Kif21b) causes a slowly progressing attrition in delivery of MCT1 to the glial-axonal junction.

The role of CNP1 in vesicular transport through myelinic channels

To test our hypothesis further, we compared myelin composition and myelinated fibre morphology in heterozygous (*Cnp1*$^{+/Cre}$) and homozygous (*Cnp1*$^{-/-}$) mutants. In optic nerves from *Cnp1* heterozygous mice, at older age (14 months), membranous structures (arrows) and dense cytoplasm (asterisks) were occasionally observed in enlarged inner tongues (Figure 6B), resembling changes in the aged CNS (Peters and Kemper, 2012). In homozygous *Cnp1* mutants, with myelinic channel collapse (Snaidero et al., 2017), axonal changes in myelinated fibres begins as early as P5 (Edgar et al., 2009) and likely underlie premature death, which occurs before one year of age (Lappe-Siefke et al., 2003). When analysing homozygous *Cnp1* mutant mice by western blotting, we found that MCT1 was strongly reduced in a myelin-enriched brain fraction by at least P75 while transcription of the encoding gene (*Slc16a1*) was similar in mutant and control brains (Figure 6C). This suggests the absence of CNP affects the delivery of MCT1 to the glial-axonal junction and/or its turnover. In support of impaired intra-myelinic transport, we found by EM of optic nerve, that in some fibres in homozygous *Cnp1* mutants, organelles appeared trapped within the myelinic channel system (Figure 6D).

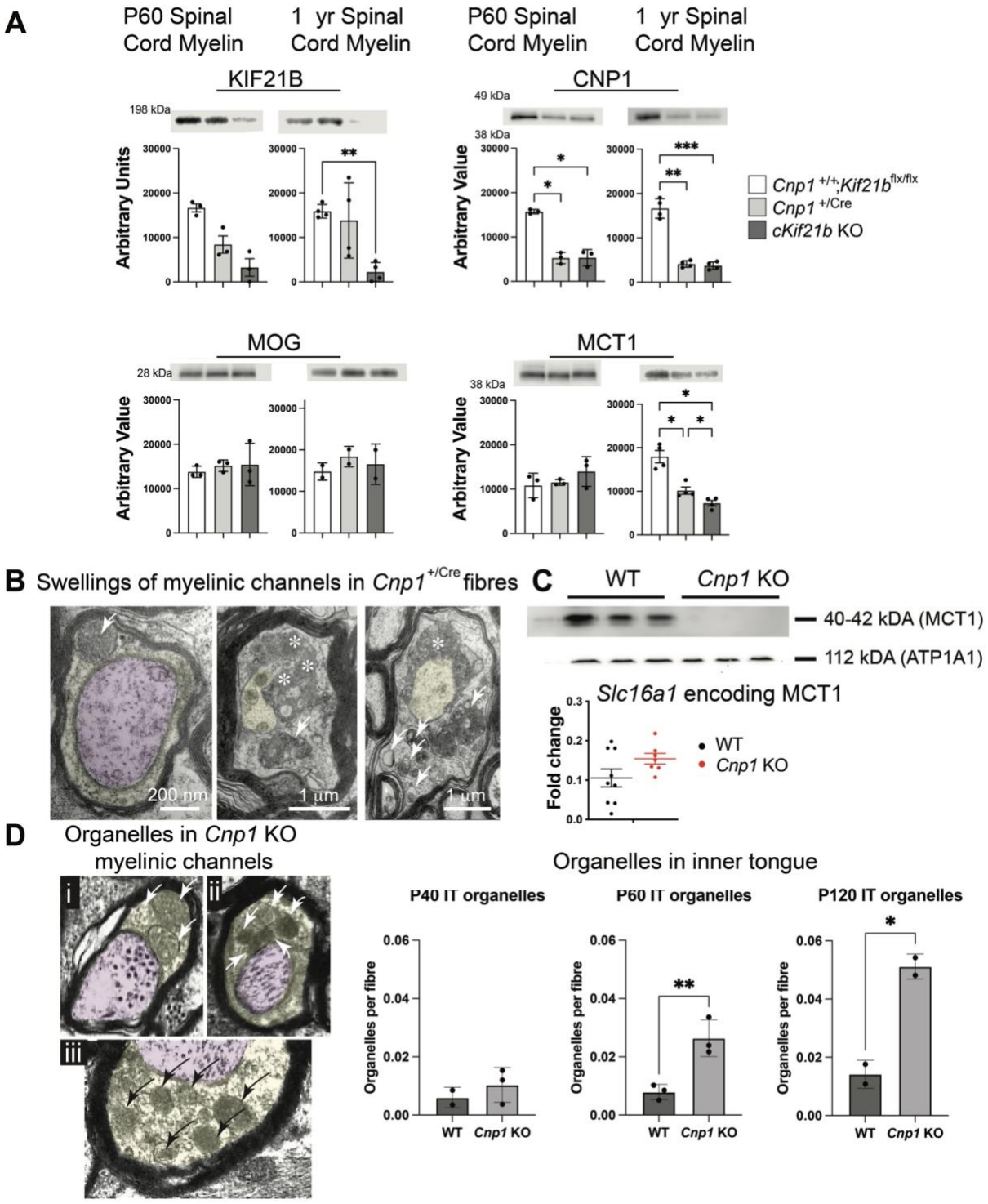

Figure 6. Monocarboxylate transporter 1 is reduced when myelinic transport is impaired.

A. Western blots of spinal cord myelin-enriched fractions of P60 and 1 year old mice. Levels of Kif21b were reduced in *Kif21b* conditional knockout (c*Kif21b* KO) mice, albeit that the reduction was not significant at P60 due to intra-group variation. Unexpectedly, levels in the *Cnp1*$^{Cre/+}$ controls (Cre cont) were highly variable. Levels of CNP1 were significantly reduced in both the *Cnp1*$^{Cre/+}$ and c*Kif21b* KO mice compared to the *Cnp1*$^{+/+}$::*Kif21b*$^{flx/flx}$ (WT) control, at P60 and 1 year. Levels of MOG were similar in all three genotypes, at both ages. At P60, MCT1 levels were similar in all three genotypes, but at 1 year of age, levels were significantly reduced in the *Cnp1*$^{Cre/+}$ mouse compared to WT control and in the *Kif21b* conditional knockout compared to both WT and *Cnp1*$^{Cre/+}$ controls.

Data were analysed using a one-way ANOVA followed by Tukey's multiple comparisons test. *: $p < 0.05$; **: $p < 0.01$; ***: $p<0.001$

B. Electron micrographs of myelinated optic nerve axons from heterozygous *Cnp1*$^{+/Cre}$ mice at age 14 months. On the left, a normal appearing paranode containing a peroxisome-like organelle (white arrow). On the right, membranous structures (arrows) and dense cytoplasm (asterisks) appear to accumulate in inner tongues in a small number of fibres. Inner tongues appear grossly swollen and impinge upon the axon.

C. Western blotting of myelin purified from homozygous *Cnp1* knockout mice shows a dramatic reduction in steady state levels of MCT1. In contrast, RT-PCR of brain lysates demonstrates no significant change in *Slc16a1* mRNA levels, when examined in relation to *Slc16a1* mRNA levels in myelin from P20 WT mouse brain, in agreement with a posttranscriptional MCT1 deficit. Data were analysed using a two tailed, unpaired Student's t test.

D. Left: Electron micrographs of myelinated optic nerve axons from homozygous *Cnp1* knockout mice, taken at (*i*) P40, (*ii*) P60 and (*iii*) P120, with undefined organelles (arrows) residing in the inner tongues (yellow overlay). **Right:** Quantitation demonstrates these organelles accumulate from age P60, i.e. long before clinical symptoms emerge at age 6 months (Lappe-Siefke et al., 2003). Bars represent mean +/- SD. Data were analysed using a two tailed unpaired Student's t-test. Data points represent mean values from electron micrographs of optic nerves of individual animals. *: $p < 0.05$; **: $p < 0.01$.

White matter ageing is associated with impaired intra-myelin transport

Advanced age is associated with altered structural integrity of myelin in white matter tracts and intracortical myelinated fibres (Mueller, 2024; Peters, 2002) and with axon vulnerability, as assessed by magnetic resonance imaging (MRI) in humans (Burzynska et al., 2024). We hypothesize that this includes the myelinic channel system, similar to its destabilization by loss of CNP. This is suggested by a peculiar interaction of *Cnp* heterozygosity and advanced brain age on behavioural symptoms in mice (Hagemeyer et al., 2012). To directly determine the effect age-related white matter changes have on intra-myelinic transport processes, we compared myelin morphology and biochemistry in wildtype mice at age 6 and 24 months. We first measured myelin inner tongue sizes across various axon diameters, observing a volume increase in the aged mice, most notably in small diameter fibres. This was accompanied by a twofold increase in fibres with organelles in the inner tongue (Figure 7A). Nonetheless, these changes were observed in the presence of an almost two-fold reduction (Fu et al., 2019; Lehotzky et al., 2010; Tokési et al., 2010) in the overall density of myelinated axons at 24

months (corpus callosum) and a doubling of axonal degeneration profiles (Figure 7B), raising the possibility that morphologically more severely affected fibres had already been lost.

When brain sections were stained for amyloid precursor protein (APP) as a marker of axonal transport impairment, we found a significant increase in APP positive swellings in the corpus callosum of 24-month-old mice (Figure 7C), but interestingly not in the cortex. These changes were accompanied by increased densities of Iba1 and Mac3 positive microglia/macrophages. Notably, by western blotting, steady-state level of MCT1 in myelin enriched fractions was approximately 50% reduced in the 24-month-old mice compared to 6-month-old controls (Figure 7D). Taken together, these data suggest that aging-associated changes of myelin integrity impairs normal transport processes in the myelinic channel system, having a profound impact on MCT1 levels, and on oligodendroglial metabolic support of axonal integrity.

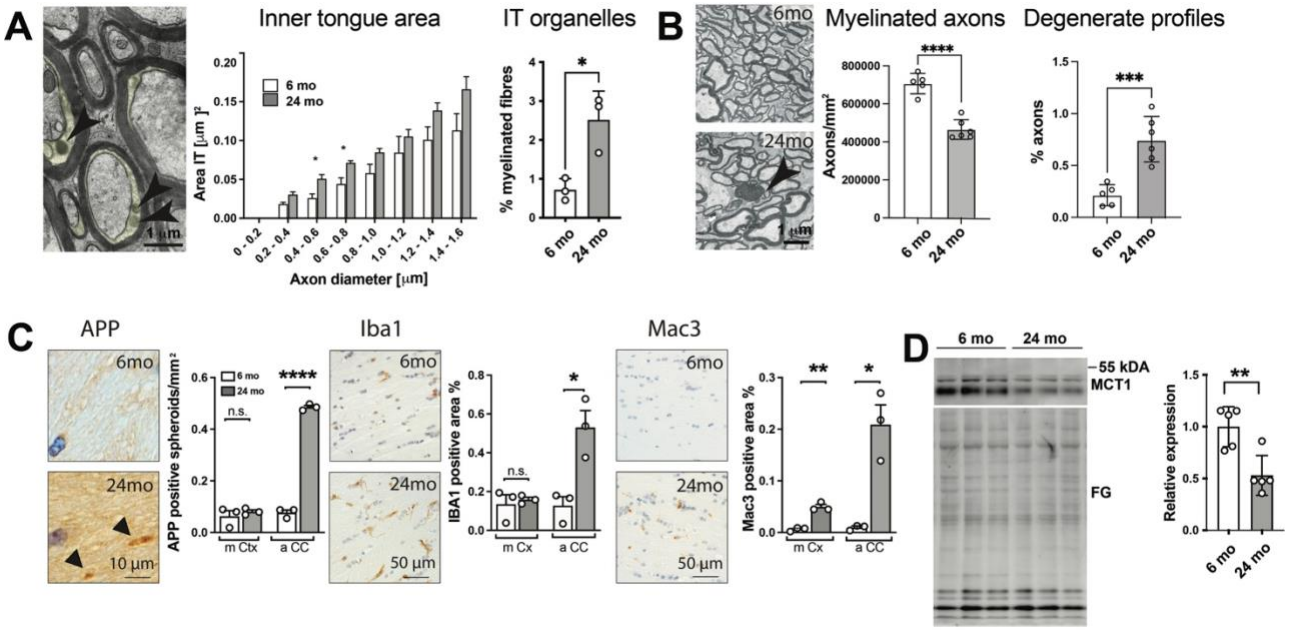

Figure 7. White matter aging leads to myelinic channels changes, decreased MCT1 levels and axon degeneration.

A. Electron micrograph of optic nerves from a 24-month-old mouse preserved by high pressure freezing (HPF), demonstrating that inner tongues (highlighted in yellow) are occasionally enlarged and are more likely to contain electron dense organelles (black arrowheads). The graphs on the right shows that inner tongue areas tended to be increased in 24-month-old animals compared to 6-month-old mice across all axon diameters (180-230 axons per nerve were examined), reaching significance

in smaller diameter fibres. Data were analysed using multiple unpaired t-tests, corrected for multiple comparisons using Holm-Šídák method (n = 5 or 6; * $p<0.05$) A higher proportion of myelinated fibres have organelles in the inner tongue (IT; n = 3). Data were analysed using an unpaired two-tailed Student's t test. * $p < 0.5$.

B. HPF EM overview showing that in 24-month-old WT mice, the density of myelinated axons is significantly reduced compared to 6-month-old mice, and the percentage of fibres with a degenerate profile is significantly increased (860-1300 axons per nerve were examined). Data were analysed by unpaired, two-tailed Student's t-tests (n = 5 or 6; *** $p < 0.001$, **** $p<0.0001$).

C. Micrographs and graphs showing that APP positive axonal swellings and Iba1-labelled microglia are increased in 24-month-old mice compared to their 6-month old counterparts in the corpus callosum (cc) but not in the motor cortex (mCtx), Bregma 0.74 mm. Mac3 positive microglia were significantly increased in both cc and mCtx in aged compared to younger mice. Data were analysed by unpaired, two-tailed Student's t-tests for each region of interest (n=3; * $p < 0.05$, ** $p<0.01$, **** $p<0.0001$)

D. Western blot showing that MCT1 is about 50% decreased in a "myelin-enriched" brain fraction from 2-year-old mice, compared to 6-month-old mice (top), using fast green (FG) as an internal standard. Data were analysed by an unpaired, two-tailed Student's t-test (n = 5; ** $p < 0.01$).

Discussion

The physiological function of compacted myelin in axonal insulation and impulse conduction is well established, but a distinct role for "non-compacted" myelin has been obscure. What is recognized by EM as non-compacted myelin was identified already at the light microscopic level by Rio de Hortega et al (1919) but suspected an experimental artifact at the time (Edgar et al., 2021). Before the application of high-pressure freezing and freeze-substitution techniques to reduce EM dehydration artifacts (Edgar et al., 2021; Möbius et al., 2016) the relative volume of inner and outer tongues was grossly underestimated. While microtubules and membranous structures were repeatedly observed in non-compacted myelin (Edgar and Griffiths, 2013) single EM cross-sections failed to show whether these are stationary remnants of development, myelin turnover or part of a vital transport system, analogous to axonal transport, between the oligodendrocyte soma and the innermost cytoplasmic myelin layer that faces the axon. Here, by combining EM, mouse genetics, live imaging of peroxisomes and pharmacological interventions, we have established the concept of motor-driven and microtubule-dependent organelle transport in established myelin sheaths, being critical for long-term axonal integrity. Moreover, *in vitro* findings demonstrating that neuronal electrical activity affects myelinic transport suggests that myelinated neurons themselves can control, at least in part, aspects of oligodendrocyte behaviour.

Our interest in these phenomena was triggered by the observation that oligodendrocytes and axons are metabolically coupled (Fünfschilling et al., 2012) through MCT1, a monocarboxylate transporter localized at the glial axonal interface (Lee et al., 2012). While it is unclear currently whether myelin turnover in adult mice rests entirely on the incorporation of new membranes at the innermost myelin layer (Meschkat et al., 2020), i.e. reflecting developmental myelination (Snaidero et al., 2014), the necessary turnover of MCT1 and its functional incorporation at the periaxonal myelin membrane would require vesicular transport to the inner tongue. We thus hypothesized that MCT1 levels in

mature myelin depend on the integrity of the intra-myelinic transport route. Our data support this suggestion by demonstrating a severe depletion of MCT1 and increased frequencies of organelles in myelin from CNP-deficient mice in which the myelinic channel system is structurally impaired (Snaidero et al., 2017); findings replicated in aged animals. In particular, the 'trapping' of myelinic organelles is reminiscent of organelle accumulations in axons upon perturbation of axonal transport (reviewed in Stassart et al., 2018).

To model and visualize transport of such nuclear-encoded membrane-bound cargoes in the myelinic channel system, we chose transgenic *Cnp-EOS*^{SKL}-mice that harbour fluorescent peroxisomes in oligodendrocytes (Richert et al., 2014). These single membrane organelles are abundant in myelinating glia and while used here as a surrogate for myelin organelles more generally, it is noteworthy that oligodendroglial peroxisomes are essential for long-term axonal integrity (Kassmann et al., 2007).

The existence of a transport system operating in mature fibres, is plausible because the myelinic channel system is developmentally derived from subcellular compartments of oligodendrocytes in which transport processes contribute directly to myelin outgrowth (Iyer et al., 2024; Nawaz et al., 2015; Snaidero et al., 2014) Analogous to neurons with growth cones, oligodendrocytes in monolayer culture have microtubules within growing cellular processes (Barry et al., 1996; Song et al., 1999) with the notable difference that these processes remain short and deliver new membranes to a flat bilayer structure that, *in vivo*, grows spirally around axons (Snaidero et al., 2014). Indeed, normal myelin sheath growth requires nucleation of microtubules, that is mediated by tubulin polymerization promoting protein (TPPP) (Fu et al., 2019; Lehotzky et al., 2010; Tokési et al., 2010). Further, mRNAs encoding myelin proteins and presumably the oligodendroglial translation machinery is transported on microtubules to the tip of the growing sheath (Brophy et al., 1993; Carson et al., 1998;

Colman et al., 1982; Holz et al., 1996; Kursula et al., 2001; Quraishe et al., 2016; Trapp et al., 1987).

In the light of our findings reported here, the importance of transport processes for developmental myelination and myelin maintenance is illustrated by the spontaneous *taiep* mutant rat, which harbours a point mutation in *Tubb4a*, encoding β–tubulin IV. This increases the ratio of "minus-end-distal" to "plus-end-distal" microtubules in the fine processes of developing oligodendrocytes (Song et al., 1999), which leads to an abnormal distribution of various myelin gene products (O'Connor et al., 2000) and hypomyelination with subsequent demyelination (Lunn et al., 1997).

Remarkably, the *Tubb4a* null mutation had no overt effect on myelination, indicating compensatory functions by other tubulins, and a dominant-negative effect of the *taiep* mutation. Nonetheless, the oligodendrocyte-specific expression of this tubulin isoform in the CNS (Schaeren-Wiemers et al., 1995) suggests that its known function as a tubulin stabilizer (Renthal et al., 1993) is important for myelinating oligodendrocytes.

A growing body of evidence has shown that neuronal electrical activity can stimulate developmental myelination (reviewed in Taylor and Monje, 2023). Less is known about axon-myelin signalling in the mature fibre, due in part to the inaccessibility of the glial-axonal junction on the inside of the myelin sheath. Our finding that the mobility of peroxisomes in myelinic channels is higher in electrically active networks, which, being a rapid response, suggests it involves direct axon-myelinic signalling. While mechanistic studies await the analysis of corresponding mouse mutants, we note that mature oligodendrocytes respond to axonal spiking activity (Yamazaki et al., 2010), at least in part through an NMDA receptor-mediated calcium rise in the myelin sheath (Micu et al., 2018) that also activates the intracellular transport of the glucose transporter GLUT1 in oligodendrocytes (Saab et al., 2016). Moreover, potassium transients in the periaxonal space of fast spiking fibres induce

$Ca2^+$ signals that stimulate glycolysis in oligodendrocytes (Looser et al., 2024).

The novelty of our findings is not the "myelinic channel system" as such, because we and others already hypothesized a "continuity" of non-compacted myelin as a cytosol-filled rim that flanks compacted myelin, with obvious reference to its developmental origin (Edgar et al., 2009, 2021; Hirano and Dembitzer, 1967; Nave, 2010b; Snaidero et al., 2014) and as a route for diffusing energy-rich metabolites for axonal support (Saab and Nave, 2017). Moreover, the same cytosolic spaces were previously visualized *ex vivo* by dye injections in both the CNS and PNS (Balice-Gordon et al., 1998; Butt and Ransom, 1989; Velumian et al., 2011). Rather, we provide the first experimental evidence that this system serves active transport processes, utilizing motor proteins and tubular tracts, exemplified by peroxisome movement. While this first description of "myelinic transport" (in analogy to "axonal transport") is necessarily incomplete with respect to the nature of the motor proteins and tubulin isoforms involved, it already helps to explain aspects of the obscure secondary axonal degeneration of myelin-specific disorders. Adult CNP-deficient mice, modelling a rare human neurological disease (Al-Abdi et al., 2020), lack integrity of this myelinic channel system, as CNP normally prevents (MBP-dependent) myelin hyper-compaction and local "channel collapse" (Snaidero et al., 2017). Consequently, nuclear encoded MCT1 of mature oligodendrocytes probably fails in the motor-driven transport via the myelinic channel system to replenish supplies at the very inner tongue of myelin as suggested by western blotting of a myelin-enriched tisse fraction. Loss of MCT1 in turn predicts poor metabolic interaction with axons (Lee et al., 2012), progressive axonal degeneration and the previously described premature death (Lappe-Siefke et al., 2003).

Clinically more relevant are myelin diseases, such as multiple sclerosis (MS), where immune-mediated attack on the myelin sheath causes progressive axon loss. We recently found that in human MS and its mouse models, a major contributor to secondary axonal degeneration is myelin injury

(Schäffner et al., 2023). We hypothesise this has the same effect on MCT1 turnover as CNP deficiency, explaining the delayed axonal degeneration occurring months after the primary lesion (Schäffner et al., 2023).

The known neuroprotective function of oligodendrocytes involves the transfer of materials from the oligodendrocyte to the axon (Chamberlain et al., 2021; Frühbeis et al., 2020; Fünfschilling et al., 2012; Lee et al., 2012; Mukherjee et al., 2020). Thus, the oligodendrocyte acts locally, at the level of each myelinated internode, to support the axon (Edgar and Garbern, 2004; Edgar et al., 2004), which, being encased in lipid-rich myelin, is physically isolated from the extracellular milieu (Nave, 2010a). At the inner tongue of normal-appearing fibres in wild-type animals, we observed multivesicular bodies, as reported previously (Frühbeis et al., 2020) and fusion profiles (Supp Figure 1G) that could empty exosomes and soluble content, respectively, into the periaxonal space for uptake by the axon.

The brain's white matter, which contains densely packed, parallel arrays of myelinated axons, is vulnerable during ageing in humans, and small diameter myelinated fibres are particularly vulnerable (Marner et al., 2003; Tang et al., 1997). If one assumes axon energy insufficiency is a pathological driver, this seems at first counter intuitive because thin axons are predicted to require less energy than thicker ones (Perge et al., 2012). A possible explanation relates to the fact that oligodendrocytes that myelinate thin axons extend many more processes than those that myelinate thick axons (reviewed in Edgar et al., 2021). As oligodendrocytes in the ageing brain can develop inclusion-containing bulbous swellings (presumably sites of transport stasis) along their processes (Peters, 2002), it becomes apparent that thin myelinated fibres might be more susceptible due to a greater risk of transport impairment in oligodendrocytes that extend numerous processes to small diameter axons.

Limitations of the study

Direct visualisation of organelle transport in myelin was conducted in an *in vitro* model of the myelinated central nervous system, in which compact myelin with an appropriate g-ratio is formed (Thomson et al., 2008), and in which multiple paranodal loops abut the axon at the paranode (Edgar et al 2021 and Supplementary Video 3). Similar to *in vivo*, these myelinating cell cultures also contain astrocytes, microglia and oligodendrocyte progenitor cells. Nonetheless, our findings should be confirmed *in vivo*.

A second limitation is that we cannot directly correlate myelin peroxisomal transport with the firing rate of the same axon. However, neurons exhibited a range of firing frequencies, which corresponds to a wide variability of myelin peroxisomes that showed movements at the time of imaging. Notably, myelin peroxisome motility was not completely blocked in the presence of TTX, but never reached the mobility seen in cell cultures with intrinsic neuronal electrical activity. Additionally, the number of organelles quantifiable in the inner tongues of myelin *in vivo* is small (estimated at ~2 per sheath) which limits our ability to quantify changes following electrophysiological stimulation. Finally, the observed loss of MCT1 in a 'myelin-enriched' spinal cord lysates by western botting provides no direct evidence that the protein is reduced at the inner lip of the myelin sheath.

Materials and methods

Mice

Conditional *Kif21b* knockout transgenic mice and 'reporter' mice harbouring for various combinations of tamoxifen-inducible PLPCreERT2 (Leone et al., 2003; Weber et al., 2001), the "stop-floxed" Cre reporter gene ß-actin-td-tomato (Madisen et al., 2010) and CNP-PexEOS2, were maintained in the Biological Services Facility at the University of Glasgow, UK, under project licence PPL P78DD6. All regulated procedures involving these animals were approved by the University of Glasgow Ethical Review Committee, licenced under the UK Animals (Scientific Procedures) Act of 1986, and conducted according to the ARRIVE guidelines. Mice were housed in standard plastic cages or within individually ventilated cages, with 1-4 littermates, and nesting domes. They were maintained with a 12-hour dark/light cycle at 19-23 ^{o}C, relative humidity 55% (+/- 10 %) and provided food and water *ad libitum*. *Tubba4* conditional knockout mice were bred and housed in the animal facility of the Max Planck Institute for Multidisciplinary Sciences (MPI-NAT). They had *ad libitum* access to water and food in standard plastic cages with 1-5 littermates in a temperature-controlled room (approx. 21°C) under a 12h/12h light/dark cycle. Animal experiments were performed in accordance with the German animal protection law (TierSchG) and approved by the Niedersächsisches Landesamt für Verbraucherschutz und Lebensmittelsicherheit (LAVES) under license 33.19-42502-04-17/2409, if subject to approval. Procedures were supervised by the animal welfare officer for the MPI-NAT, Göttingen, Germany. The animal facility is registered at the MPI-NAT is registered according to §11 Abs. 1 TierSchG. CD-1 mice were purchased from Charles River Laboratories (Margate, UK) and housed at the University of Nottingham with *ad libitum* access to food and water, temperature 22–23°C, and a 12 h:12 h light–dark cycle.

Transgenic reporter mice: Male and female pairs, which together harboured one copy of each of three transgenes, were mated/time-mated to produce embryos/offspring harbouring combinations of

transgenes encoding tamoxifen-inducible PLPCreERT2 {Leone, 2003 7898 /id; Weber, 2001 7163 /id}, the "stop-floxed" Cre reporter gene ß-actin-td-tomato {Madisen, 2010 10467 /id} and CNP-PexEOS2 {Richert, 2014 10701 /id}. Approximately one in eight embryos/offspring harboured all three transgenes leading to the expression of EOS2 +ve peroxisomes in td-tomato +ve oligodendrocytes.

Kif21b conditional knockout mice (Muhia et al., 2016): By intercrossing *Kif21b*$^{lacZ/neo}$ mutants with mice expressing FLIP recombinase (129S4/SvJaeSor-*Gt(ROSA)26Sor*$^{tm1(FLP1)Dym}$*/J*; backcrossed into C57BL/6N for at least 10 generations) (Farley et al., 2000) the lacZ/neo cassette was excised *in vivo*, yielding the "conditional ready" heterozygous flox allele in mice carrying the *Kif21f* KIF21b$^{tm2a(KOMP)Wtsi}$ allele (also termed *Kif21b*$^{flox/+}$). *Tubb4a*$^{flox/+}$ mice were subsequently bred to homozygosity. To inactivate expression of *Kif21b* in oligodendrocytes, homozygous mice were crossed with mice expressing *Cre* under the control of the *Cnp* promotor (*Cnp*$^{tm1(cre)Kan}$) (Lappe-Siefke et al., 2003) to generate *Cnp*$^{+/Cre}$::*Kif21b*$^{fl/fl}$; *Cnp*$^{+/Cre}$::*Kif21b*$^{+/+}$ or *Cnp*$^{+/Cre}$::*Kif21b*$^{+/+}$; or *Cnp*$^{+/+}$::*Kif21b*$^{fl/fl}$ offspring.

Tubb4a conditional knockout mice: Embryonic stem cell clones HEPDD0853_6_E02 and HEPD0853_6_B04 harboring the tubulin beta 4A class IVA *Tubb4a*$^{tm1a(EUCOMM)Hmgu}$ 'knockout-first' allele (reporter-tagged with conditional potential) of the Tubb4a gene with exons 2 and 3 flanked by loxP sites were obtained from the European Mouse Mutant Cell Repository (EuMMCR, Munich, Germany) and microinjected into blastocysts by standard procedures. Highly chimeric animals were crossed to C57Bl/6N females yielding *Tubb4a*$^{tm1a(EUCOMM)Hmgu}$ mutant mice (also termed *Tubb4a*$^{lacZ/neo}$*)*. By intercrossing *Tubb4a*$^{lacZ/neo}$ mutants with mice expressing FLIP recombinase (129S4/SvJaeSor-*Gt(ROSA)26Sor*$^{tm1(FLP1)Dym}$*/J*; backcrossed into C57BL/6N for at least 10 generations) (Farley et al., 2000) the lacZ/neo cassette was excised *in vivo*, yielding the "conditional ready" heterozygous flox allele in mice carrying the *Tubb4a*$^{tm1c(EUCOMM)Wtsi}$ allele (also termed *Tubb4a*$^{flox/+}$). *Tubb4a*$^{flox/+}$ mice were subsequently bred to homozygosity. To inactivate expression of

Tubb4a in oligodendrocytes, the loxP flanked exons 2 and 3 were excised *in vivo* upon the generation and appropriate intercrossing of *Tubb4a*$^{flox//flox}$ mice with phenotypically normal *Tubb4a*$^{+/+::}$*CNP*$^{Cre/+}$ mice that expressed *Cre* under the control of the *Cnp* promotor (*Cnp*$^{tm1(cre)Kan}$) (Lappe-Siefke et al., 2003).

For optic nerve electrophysiology, CD-1 male mice (weight 28–35 g, corresponding to 30–45 days of age) were purchased from Charles River Laboratories (Margate, UK) and housed at the University of Nottingham with *ad libitum* access to food and water and temperature 22–23°C, on a 12 h:12 h light–dark cycle. Mice were killed by Schedule 1 cervical dislocation; death was confirmed by permanent cessation of the circulation. Experiments were approved by the University of Nottingham Animal Care and Ethics Committee and carried out in accordance with the Animals (Scientific Procedures) Act 1986 under appropriate authority of establishment, project and personal licences.

a-MCT antibody: from Kathrin Kusch, Rabbit, polyclonal, 1:1000

Genotyping

Routine genotyping was performed by genomic PCR on ear clip DNA. Ear notches were each lysed in 100 µL 50 mM NaOH at 95ºC for 90 minutes, then neutralized with 10 µL 1M Tris buffer (pH 5) followed by thorough vortexing.

Tubb4a^{+} *and Tubb4a*^{flox} alleles were detected using sense primer P1 (5’-GAC AGT CAG CAA CTG AAG AAG TGG C-3’) together with antisense primer P2 (5'-CTG TTG TCA ATC TTG GCC ATG AGC C-3') and P3 (5'-TGA ACT GAT GGC GAG CTC AGA CC -3') amplifying a 546 bp product for the WT allele, a 748 bp product from the flox allele, and a 674 bp product from the recombined flox allele.

Cnp^{Cre} *and Cnp*^{wt} alleles were identified by genomic PCR with primers P4 (5'-GCC TTC AAA CTG TCC ATC TC-3'), P5 (5'-CCC AGC CCT TTT ATTA CCA C-3'), and P6 (5'-CAT AGC CTG AAG AAC GAG A-3') amplifying a 700 kb product from the wt allele and a 400 bp product from the Cre or with *Cnp1* Sense 5$^{/}$-GCC TTC AAA CTG TCC ATC TC-3$^{/}$, Cnp1N2 5$^{/}$-GAT GGG GCT TAC TCT TGC-3$^{/}$ and Puro3 5$^{/}$-CATAGCCTGAAGAACGAGA-3$^{/}$, amplifying a 1180 bp and 894 bp products for Cnp1^{WT} and Cnp1^{Cre}, respectively.

Mice expressing tamoxifen-inducible td-tomato fluorescent protein and mEOS2-lableled oligodendrocyte peroxisomes were genotyped using the following primers:
Tom Fw 5$^{/}$ TAC GGC ATG GAC GAG CTG TAC AAG TAA-3$^{/}$ and Tom Rv 5$^{/}$ CAG GCG AGC AGC CAA GGA AA-3$^{/}$, yielding an ~500bp product.

EOS Fw 5$^{/}$-CTT CTT ACA CAG GCC ACC ATG AGT GCG-3$^{/}$ and EOS Rv 5$^{/}$-GGA TCC TTA CTT AGT TAA AGC TTG GAT CGT-3$^{/}$, yielding an ~800bp product.

PLP1 Fw 5$^{/}$ TGG ACA GCT GGG ACA AAG TAA GC and PLP Rv 5$^{/}$ CGT TGC ATC GAC CGG TAA TGC AGG C-3$^{/}$ yielding an ~250 bp product.

Kif21b^{+} and *Kif21b*^{flox} alleles were identified by genomic PCR with primers Fw Kif 83 5$^{/}$-GGA CAT GAT GGT GAT TTA GAG G-3$^{/}$ and Rv Kif84 5$^{/}$-AAA CCT GGG CAA AGG CAT AC-3$^{/}$ yielding 825 bp (WT) and 970 bp (flox allele) products.

Transmission electron microscopy of conventionally fixed tissue

Transcardiac perfusion of mice was performed under the effect of a lethal dose of Avertin or Dolethal. For transmission electron microscopy (TEM), mice were perfused with 4% paraformaldehyde (PFA), 2.5% glutaraldehyde in 0.1 M phosphate buffer, postfixed in 4% PFA overnight and subsequently transferred to 1% PFA (conditional *Tubb4a* knockout mice and controls) or with 4% PFA and 5% glutaraldehyde in cacodylate buffer, and postfixed in the same for 24 hours to three weeks

(conditional *Kif21b* knockout mice and controls). Optic nerves were subsequently dissected and processed for electron microscopy, as described (Edgar et al., 2020).

Following electrophysiology of CD1 mouse optic nerves, paired nerves (stimulated and non-stimulated) were immersed in 4% PFA and 5% glutaraldehyde in cacodylate buffer for at least one week and processed and sectioned as above. Morphometry and quantification of electron micrographs were performed using Fiji (Schindelin et al., 2012).

Transmission electron microscopy of high pressure frozen tissue

Tissue was collected and processed as described in (Möbius et al., 2016).

White matter morphometry

Optic nerve cross sections taken mid-way between the retina and the extraorbital region of the nerve were imaged at 12000 x on a JEOL 1200 EX transmission electron microscope (c*Kif21b* and c*Tubba4* ko mouse optic nerves) or an EM912AB electron microscope (aged mice). Images of optic nerve cross section were captured randomly at 12,000x magnification using Olympus ITEM Software (12-20 images per nerve, each ~74 μm^2) or at 3150x (5 images per nerve, each 480 μm^2) using the ImageSP software (TRS, SysProg, ImageSP, vers1.1.4.62), respectively. Images were opened in Fiji (Schindelin et al., 2012), and the relevant feature was counted using the Image J Cell Counter plug-in within and on west and south borders of an area of interest (AOI), by a blinded experimenter. The sum of the counts from all micrographs from a single nerve was converted to numbers per mm^2. Some counts were converted to fibres per nerve after measuring the area of the optic nerve cross section from toluidine blue stained resin sections. For quantifying organelles in inner tongue and paranodal loops, dense organelles (Figure 1) were identified, and the numbers of organelles was divided by the number of myelinated fibres to determine the number of organelles per fibre cross-section. To

determine organelle diameter, the area of each organelle was measured in Fiji (Schindelin et al., 2012) by tracing the organelle bounds and the diameter calculated, assuming the area was circular. Organelles were assumed to be spherical, and the maximum diameter observed on optic nerve cross sections was assumed to represent the maximum diameter in the longitudinal direction (along the sheath).

Tissue collection for light microscopy (frozen sections)

Mice were perfusion fixed under the effect of a lethal dose of Dolethal.with 0.9% saline followed rapidly by 4% PFA and immersed in 4% PFA for a minimum of 24 hours before the optic nerve and spinal cord were dissected. Dissected tissues were transferred into 20% sucrose in PBS until they sank. Tissues were frozen in OCT (Sakura Finitek, Torrance, CA, USA) in liquid nitrogen-chilled isopentane. Ten µm thick sections were cut on a cryostat (Bright Instruments) and mounted on Colorfrost Plus charged slides (Thermo Fisher Scientific). Tissue sections were permeabilised in methanol for 10 minutes at -20 ^{o}C and immunostained with rabbit anti-Caspr1 (kindly gifted by Professor Ori Peles) by incubation overnight at 4 ^{o}C in blocking buffer (10% goat serum, 1% bovine serum albumin (BSA), 0.1% Tween, 0.9 % NaCl in PBS). Bound primary antibodies were detected using Alexa 647 goat anti-rabbit IgG (1:1000; Invitrogen).

Tissue collection for light microscopy (paraffin sections)

Mice were anesthetized with a lethal dose of avertin and perfused through the left ventricle with Hanks balanced salt solution followed with 4% paraformaldehyde in 0.1 M phosphate buffer. The brains were dissected, post-fixed overnight in 4% PFA, paraffinized using a Microm STP 120 Spin Tissue Processor (Thermo Scientific) and subsequently embedded in paraffin blocks on a HistoStar

embedding workstation (Epredia).

Immunohistochemistry and quantification on paraffin sections

Five µm brain sections in paraffin were cut on a RM2155 (Leica) rotary microtome and mounted on Histobond adhesive microscope slides. Slices were deparaffinized at 60°C and rehydrated using xylene and a descending ethanol series. For heat-induced epitope retrieval, sections were treated in sodium citrate buffer (0.01 M, pH 6.0) in a 400-Watt microwave for 10 minutes, followed by a 20-minute cooldown period. For immunohistochemical antibody detection using a chromagen, endogenous peroxidase activity was blocked with 3% hydrogen peroxide. Subsequently, sectons were blocked for 1 h at RT in 20% goat serum in PBS and incubated with primary antibodies (anti-MAC3, anti-Iba1, anti-APP) at 4°C overnight. The LSAB2 system-HRP kit (DAKO) was use and the HRP substrate 3,30-Diaminobenzidine (DAB) was applied using the DAB Zytomed kit (Zytomed Systems GmbH). Nuclei were labeled by Hematoxylin stain. Imaging was performed using a Zeiss Axio Imager Z1 bright-field light microscope equipped with a Zeiss AxioCam MRc camera using ZEN 2012 blue edition software. Images of anterior corpus callosum and motor cortex (Bregma 0.74 mm) were color deconvoluted using the “Color Deconvolution” (1.3) plugin in Fiji/ImageJ. Iba1^{+} and MAC3^{+} areas were quantified using thresholding, and APP spheroids were quantified manually using the “Cell counter” plugin from Fiji/ImageJ. All data were normalized to the respective quantified areas.

Quantitative RT-PCR

RNA was extracted from brain lysates and purified myelin-enriched fractions using the miRNeasy Mini Kit (Qiagen) and the concentration was increased using Co-precipitant pink (Bioline), if necessary. The purity and concentration of RNA was evaluated using a NanoDrop spectrophotometer and RNA Nano (Agilent). cDNA was synthesized using Superscript III (Invitrogen, Carlsbad, CA, USA) according to the manufacturers' instructions. Quantitative RT-PCR (qRT-PCR) was performed

in triplicates with the GoTaq qPCR Master Mix (Promega) on a LightCycler 480 Instrument (Roche Diagnostics). Expression values were normalized to the mean of the house-keeper genes *Atp1a1*, *Hprt* and *Rplp0*. Relative expression changes were analyzed using the 2ΔΔC(T) method, normalized to mean expression in P20 wildtype myelin-enriched fractions (set to 1). All primers were designed with Universal Probe Library from Roche Applied Systems (https://www.roche-applied-science.com) and validated with NIH PrimerBlast. All primers were intron-spanning. Primers were specific for *SCL16a1/Mct1* (forward 5'-GGATATCATCTATAATGTTGGCTGTC-3', reverse 5'-GCTGCCGTATTTATTCACCAA-3'; Atp1a1 (Forward 5'- GGCCTTGGAGAACGTGTG-3', Reverse 5'-TCGGGAAACTGTTCGTCAG-3'); Hprt (Forward 5'-CCTGGTTCATCATCGCTAATC-3', Reverse 5'-TCCTCCTCAGACCGCTTTT-3') and Rplp0 (Forward 5'- GATGCCCAGGGAAGACAG-3', Reverse 5'-ACAATGAAGCATTTTGGATAATCA-3').

Tissue collection and western blotting of myelin-enriched fraction and optic nerves

Male c57Bl6/N wildtype mice and CNP null mutant mice ($Cnp^{tm1(cre)Kan}$; Lappe-Siefke et al., 2003) from breeding colonies at the Max Planck Institute of Multidisciplinary Sciences and male and female $Cnp1^{+/+}$::$Kif21b^{flx/flx}$, $Cnp1^{+/Cre}$::$Kif21b^{+/+}$ or $Kif21b^{+/flx}$ and $Cnp1^{+/Cre}$::$Kif21b^{flx/flx}$ from breeding colonies at the University of Glasgow were used. A light-weight membrane fraction enriched for myelin was purified from mouse brain hemispheres or spinal cords, as described (Erwig et al., 2019). Optic nerves were homogenised in ROLB Buffer, pH 7.4 (10 mM HEPES, 50 mM NaF, 25 mM $Na_4P_2O_7$, 80 mM KH_2PO_4, 5 mM EDTA and 1% SDS with protease inhibitor) using a plastic pestle and mortar then centrifuged at 16,000g for 10 minutes, 4ºC and the soluble fraction was aspirated. Protein concentration was determined using the DC protein assay (BioRad) or a BCA Protein Assay Kit (Thermo Fisher) according to the respective manufacturer's instructions. Immunoblotting of brain 'myelin' was performed as described (Späte et al., 2024). Spinal cord 'myelin' and optic nerve samples were resolved on 4-12% Bis-Tris geld at 200 V and transferred onto PVDF membrane using

either semi-dry method (Trans-blot; BioRad) or a wet gel transfer (Mini Trans-blot; BioRad). Semi-dry transfers were run at 1.3 mA/cm^2 for 1 h +/- 15 minutes and wet gel transfers were run overnight at 35 V or for 1 hour at 100 V. Membranes were blocked with 5% milk in Tris buffered saline with 0.01% Tween 20 then incubated in primary antibody in blocking buffer overnight at 4°C. Primary antibodies were specific for SCL16a1/MCT1 (1:50-1:1000, Stumpf et al., 2019), ATP1a1 (1:2000; Abcam) KIF21b (1:50; HPA027274, Sigma; adsorbed against *Kif21b* knockout brain tissue), CNP (1:2000; ab6319, Abcam), MOG (1:2000; gifted by Professor Christopher Linington), and β-Actin (1:5000; A1978, Sigma). Membranes were thoroughly washed (1X TBS/T) and binding was detected using appropriate peroxidase conjugated secondary antibody (Anti-mouse/rabbit IgG HRP-linked, Cell Signalling Technologies), wash repeated then incubated for 1 minute in WesternBright^{TM} ECL mix (K-12045-D20, Advansta). Immunoblots were scanned using the Intas ChemiCam system or using the Li-Cor C-DiGit blot scanner.

Myelinating cell cultures

Pregnant 'reporter' mice were killed on embryonic day 13 (E13; day of plug being E0) by cervical dislocation followed by exsanguination or CO_2 exposure followed by cervical dislocation. Following removal of the uterine horns, isolation of the embryos and spinal cord removal, all embryonic cords were pooled and used to generate a single cell suspension for culture, as described (Bijland et al., 2019) resulting in a population of cells with a mixed genotype. Myelinating cultures were maintained for up to 50 days *in vitro* (DIV), in a cell culture incubator at 37°C in humidified 5% CO_2. One µM (final) 4-hydroxy tamoxifen was administered for 1 hour on DIV 21 +/- 3 days to induce td-tomato expression in a subpopulation of oligodendrocytes.

Neuronal cell cultures

These were established as for myelinating cell cultures (Bijland et al., 2019), except that the dissociated spinal cord cells were plated in 80 µL serum-containing plating medium (50% DMEM, 25 % HBSS and 25 % horse serum) at 80.0000 cells per well in Seahorse XFp Miniplates (Agilent, 103025-100). After two hours, the serum-containing media was removed and replaced with 125 µL Neurobasal medium (Gibco, A2477501) supplemented with B-27 (Gibco, 17504044), 10 µM 5-Fluoro-2′-deoxyuridine (FDU; Sigma-Aldrich, 343333), 10 ng nerve growth factor (NGF; Sigma-Aldrich, N6009), 10 mM glucose (Agilent, 103577-100), 0.5 mM glutamine (Agilent, 103579-100), 0.227 mM pyruvate (Agilent, 103578-100). The cells were maintained until DIV 15 +/- 1 day and media was changed every 2 days.

Seahorse neuromodulator assay on neuronal culture

The cartridges for the Seahorse XF Bioanalyser (Agilent) were prepared according to the manufacturer's instructions. On the day of the assay, Neurobasal media was changed to 180 µL of the Seahorse assay medium (Agilent, 103680-100, supplemented with 2 mM glutamine, 1 mM pyruvate and 10 mM glucose) and equilibrated in a non-CO_2 incubator for 1 h at 37ºC. The assay was as follows: 3 cycles of baseline measurements were followed by injection of 100 µM Picrotoxin and two measurement cycles, followed by injection of 1 µM TTX and 2 measurements cycles. The total duration for the assay was 40 minutes and oxygen consumption rate (OCR) and extracellular acidification rate (ECAR) were recorded. The OCR and ECAR values for each phase were averaged and plotted over time.

Treatment of myelinating cultures with nocodazole

On DIV27 +/- 3 days, myelinating cultures were treated for 3 hours at 37ºC in a humidified 5% CO_2 incubator with nocodazole (final concentration 20 µM; 1.2 µL of 5 mg/mL in DMSO was added per 1 mL media; SML1665; Sigma-Aldrich).

Treatment of cultures with neuromodulators

On DIV29 +/- 5 days, myelinating cultures were treated for ≥ 5 minutes with either picrotoxin (PTX) (final concentration 100 µM; 1 µL stock solution in DMSO in 1 mL media; P1675; Sigma-Aldrich), tetrodotoxin (TTX) (final concentration 1 µM; 1 µL stock solution in water in 1 mL media; 1078; Tocris, Abingdon, UK) or N-methyl-D-aspartic acid (NMDA) (final concentration 100 µM; 1 µL stock solution in PBS in 1 ml media 0114; Tocris, Abingdon, UK). A DMSO-only control was conducted for comparison with PTX. To block NMDA receptor activation, cultures were treated with 7-Chlorokynurenic acid (7-CKA) (final concentration 50 µM; 1 µL stock solution in DMSO in 1 mL media; ab120024; Abcam) and D-AP5 (final concentration 100 µM; 1 µL stock solution in water in 1 mL media; ab120003; Abcam) and incubated for 80-90 minutes at 37ºC in humidified 5% CO_2. Cultures were then treated with 1 µM TTX for ≥ 5 minutes and then with 100 µM NMDA ≥ 5 minutes.

Live imaging of cell cultures

For live imaging, myelinating cultures were plated on custom-made imaging dishes, prepared from 35 mm diameter Petri-dishes (353001; Falcon), with three x 8 mm diameter circular holes in the base and a 25 mm diameter glass coverslip (630-2213; VWR) glued underneath (Bijland et al., 2019). Live td-tomato rendered oligodendrocytes with EOS2-lablled peroxisomes were imaged using an inverted Zeiss Observer Z1 Spinning Disc confocal microscope, equipped with a Yokogawa CSU-X1 filter wheel and spinning disc unit, a Photometrics Evolve 512 delta EM-CCD camera, with 488 nm (300-600 ms exposure, 4-9 % power) and 568 nm (200-400 ms exposure, 4-6% power) laser lines and a 63x/1.4 Oil Pln Apo objective and Zen software (2012, Blue Edition). Alternatively, an inverted Leica DMi8 widefield microscope, with a Hamamatsu ORCA-Flash4.0 V3 Digital camera C13440-20C, HC PL APO CS2 63x/1.40 Oil objective, and LAS-X software (version 3.7.1) or an inverted Zeiss Observer Z1 epi-fluorescence microscope equipped with an AxioCam MRc3, ×0.63 Camera Adaptor, ZEN 2012 blue edition software using a Zeiss plan-apochromat 63 × 1.4 oil objective, were

used. Cells were maintained at 37ºC on a heated stage insert and gassed with humidified 5% CO_2 to maintain physiological pH, which was monitored on the basis of the colour of the phenol red-containing cell culture media. To record peroxisome movement, frames were captured every 10 seconds over a 10-minute period, in the 568 (td-tomato) and 488 (EOS2) channels.

Quantification of peroxisome motility

All quantification was performed blinded using time-lapse images of td-tomato +ve, myelinating oligodendrocytes containing EOS2-labelled peroxisomes. Numbers of peroxisomes in oligodendrocyte processes or sheaths were counted manually using the multi-point tool in Fiji (Schindelin et al., 2012). To calculate the percentage of motile peroxisomes in oligodendrocyte processes or sheath, the total number of peroxisomes and the number of motile peroxisomes were recorded. Peroxisomes that moved >3 µm were considered 'motile' and cells were excluded if there were <5 myelin peroxisomes observable in the time-lapse image. To measure the distances travelled by the motile peroxisomes, the 488 (EOS2) channel of the time-lapse images was analysed using the Simple Neurite Tracer plugin (https://imagej.net/plugins/snt/) with Fiji. Time lapse frames were converted into an AVI file, and the point tool in Simple Neurite Tracer was used 'mark' the position of the peroxisome at each frame, and distances travelled between frames, including bidirectional movements, were summed. Average speed of each peroxisome was calculated by dividing the total distance travelled (µm) by time (seconds). Motile speed was calculated by dividing the total distance travelled by the number of frames in which the peroxisome was motile.

For motile peroxisomes in processes (between the soma and the sheaths), the direction of movement in relation to the cell body was also recorded, and the net distance travelled in each direction (anterograde or retrograde) was quantified. First, the length of each process was measured using the Simple Neurite Tracer plugin. Second, as process lengths varied, and hence, impacted distance

available, the distance travelled by each peroxisome (measured as above) was normalised to distance per 100 µm process. Third, to calculate the net movement in the anterograde or retrograde direction per process, the normalised distance travelled per peroxisome was multiplied by 1/total number of peroxisomes per process (including stationery ones) and then the distances in either direction were summed. If there were no motile peroxisomes in a process, zero was recorded for both anterograde and retrograde movement. If there was movement in only one direction, zero was recorded for the opposite direction. For example, for a process with 5 peroxisomes, of which 1 moved 50 µm per 100 µm in the anterograde direction, the net distances were defined as anterograde: 1/5 x 50 µm = 10 µm per 100 µm and retrograde: 0 µm per 100 µm.

Culture on nanofibres

Spinal cords were dissected from postnatal day 3-5 (P3-5) 'reporter' mice, digested using trypsin (0.125%) in HBSS minus Ca^{2+} and Mg^{2+}, and dissociated into a single cell suspension by trituration through 21 and 23 G needles. Only glial cells survive this process, eliminating almost all neurons from the cell culture. Cells were plated at 50,000 cells per well on 4 µm diameter Poly-L-Lactic Acid (PLLA) electrospun fibers in 12-well cell crown scaffolds (The Electrospinning Company) in serum-containing plating medium (see Myelinating Cultures). The following day, the plating medium was removed and the glial cells were maintained in Sato's medium (DMEM, glucose [25 mM], pyruvate [1 mM], penicillin/streptomycin [1% v/v], apo-transferrin [5 µg/ml], sodium selenite [5 ng/ml], insulin [5 µg/ml], putrescine [16 µg/ml], progesterone [7.3 ng/ml], T3 [0.5 nM] and horse serum [1% v/v]), with media replenished 50:50 every 7 days.

Immunocytochemistry

Cell cultures were fixed in 4% PFA at room temperature (RT) for 10 minutes, or by the addition of 8% PFA (37°C) to cell culture media (1:1 v:v), then permeabilised for 10 minutes in either 0.5% triton

X at RT or in absolute methanol at -20ºC. Following washes in PBS, blocking buffer (10% goat serum, 1% bovine serum albumin (BSA), 0.1% Tween, 0.45 g NaCl in 50 mL PBS) was applied for 1 hour at RT and then cells were incubated overnight in primary antibody at 4ºC, in 10% goat serum in PBS or blocking buffer. After thorough washing, secondary antibodies were applied at 1 in 1000 for ~1 hour at RT. Finally, cells were washed in PBS and rinsed in water, then coverslips were mounted on glass slides in Mowiol containing DAPI (2 µg/ml; Invitrogen). For immunocytochemistry of microtubules, cells were first incubated for 1 minute with pre-warmed extraction buffer (0.3% Triton X and 0.1% glutaraldehyde in BRB80 buffer (BRB80 buffer: 80 mM Pipes, 1mM EGTA and 4 mM $MgCl_2$, pH 6.8) (Jansen et al., 2021) then fixed for 10 minutes in 4% PFA/PBS and permeabilised for 10 minutes in 0.25% Triton-X before blocking for 1 hour in 3% BSA/PBS at RT. Cells were next incubated for 1 hour with primary antibody at RT, diluted in 3% BSA/PBS, washed in PBS, then incubated for 1 hour at RT with secondary antibodies diluted in 3% BSA/PBS. Coverslips were washed and mounted as described above. Primary antibodies were; mouse IgG1 anti-β tubulin IV (1 in 400; ab11315; Abcam), rat anti-MBP (1 in 800; ab7349; Abcam), mouse IgG1 anti-CNP (1 in 800; ab6319; Abcam), rabbit anti-Caspr (1:1000; kindly provided by Professor E Peles), mouse IgG2a anti-Ermin (1:500; MABN323; Merck); mouse IgG3 anti-tyrosinated tubulin (1:300; T9028; Merck); mouse IgG2b anti-acetylated tubulin (1:300; T7451; Merck); rabbit anti-detyrosinated tubulin (1:300; ab48389; Abcam). Bound primary antibodies were detected using Alexa 488, 568 or 647 goat anti-mouse IgG, IgG1, IgG2a, goat anti-rabbit IgG or goat anti-rat IgG (1:1000; Invitrogen).

To stain cells cultured on nanofibres, the nanofibre crown was transferred between wells of a 12-well dish for permeabilization of cells, antibody incubations and washing, as above. The nanofiber crowns were placed on glass slides and the fibres were sandwiched between the slide and a 13 mm glass coverslip, using Mowiol with DAPI. The crown was removed 2 days later, after the Mowiol had

hardened, as described (Bechler, 2019).

Transfection with sensors of microtubule post translational modifications (PTMs)

Myelinating cultures were incubated with DharmaFECT 1 transfectant reagent (T-2001-01; Horizon) according to manufacturer's instructions and with 1.125 µg/mL tyrosinated tubulin sensor TagRFP-T AlaY1 (158751; Addgene) (Kesarwani et al., 2020) or Stable Microtubule-Associated Rigor-Kinesin (Jansen et al., 2023) for 9 hours. Cells were immediately fixed in 4% PFA/PBS and immunostained as described in 'Immunocytochemistry'.

Fluorescence Microscopy

Fixed cell cultures and tissue sections were generally imaged with an inverted Zeiss Observer Z1 epi-fluorescence microscope equipped with an AxioCam MRc3, x0.63 Camera Adaptor, ZEN 2012 blue edition software using Zeiss plan-apochromat 63 x 1.4 oil objective. High resolution images were taken using a Zeiss LSM 880 confocal microscope or Zeiss Z.1 AxioImager with ApoTome attachment, using Zen software and Plan-Neofluar 40x/1.30 oil objective or Plan-Neofluar 63x/1.30 oil objectives. Cells on nanofibres were imaged on an Olympus IX70 microscope, QIcam Fast digital camera (QImaging Surrey, BC, Canada) and Image-Pro Plus 6 software (Media Cybernetics, Silver Spring, MD).

Quantifying peroxisomes in paranodes

Myelinating cultures were treated with neuromodulators, TTX or PTX (see Treatment of Cultures with Neuromodulators) for 5 minutes, then immediately fixed in 4% PFA/PBS (10 minutes) and either immunostained with anti-CNP (see Immunocytochemistry) and mounted on glass slides in Mowiol or mounted in Mowiol without immunostaining when expressing td-tomato. Following blinding, coverslips were scanned in the green (EOS2-labelled peroxisomes) and red (oligodendrocytes stained

with anti-CNP or labelled with td-tomato) channels, and oligodendrocytes with EOS2-peroxisomes in the soma were selected at random. A z-stack (0.32 μm steps) was captured of paranodal regions using a Zeiss Observer Z1 epi-fluorescence microscope. Numbers of peroxisomes in each paranode were counted manually in Fiji or in Zen 2012 (Blue edition) in a minimum of 10 paranodes per treatment.

Electrophysiology of optic nerve

Following decapitation, the optic nerves were cut behind the eye orbit then exposed by lifting the cerebral hemispheres rostro-caudally. They were cut at optic chiasm (5-7 mm length) and gently freed from their dural sheaths then placed in an interface perfusion chamber (Medical Systems, Greenvale, NY, U.S.A.), as described (Stys et al., 1991). Optic nerves were maintained at 37°C using a TC-202A bipolar temperature controller (Digitimer, Welwyn Garden City, UK) and perfused with artificial cerebrospinal fluid (aCSF) that contained (in mM): 153 Na^+, 3 K^+, 2 Mg^{2+}, 2 Ca^{2+}, 143 Cl^-, 26 HCO_3^-, 1.25 HPO_4^{2-}, and 10 glucose. The aCSF was bubbled with a gas mixture (95% O_2: 5% CO_2) to maintain pH at 7.45. Tissue was oxygenated by a humidified gas mixture (95% O_2: 5% CO_2) that flowed over its surface. Nerves were allowed to equilibrate for 30 minutes then a stimulating suction electrode back-filled with aCSF was attached to the proximal end of one nerve. A recording electrode filled with aCSF was attached to the distal end of the same nerve to record the CAP, which was evoked by a 125% supramaximal stimulus (30 μs in duration: a Grass S88 stimulator connected to two SIU5 isolation units in parallel capable of delivering two independently controllable pulses). Nerves were stimulated at 50 Hz for 20 minutes. CAPs were recorded from a suction electrode attached to the distal end of the nerve connected to an SR560 low noise preamplifier (Stanford Research Systems, Sunnyvale, CA 94089, USA): the signal was amplified up to 1000x and filtered at 30 kHz. The differential output was fed into a HumBug Noise Eliminator (Digitimer Ltd, Welwyn Garden City, UK) to remove mains frequency noise (50 Hz). The signal was acquired via an Axon

Digidata 1550B using Clampex 11.3 (Molecular Devices Ltd, Wokingham, Berkshire, UK). The control nerve remained untouched on the perfusion chamber, and when the stimulation protocol was completed, both nerves were transferred rapidly to fixative as described in 'Tissue collection and fixation for electron microscopy'.

Electrophysiology of myelinating cultures

Myelinating cultures were transported between sites at room temperature in a sealed box containing humidified 5% CO_2 (maximum journey time 1.5 hours) and allowed to equilibrate at least 1 hour in cell culture incubator (37ºC, 5% CO_2). One glass coverslip at a time was removed from the cell culture media dish and placed in a clean 35 mm diameter Petri dish containing pre-warmed extracellular solution, then viewed using an Olympus IX71 inverted microscope with epifluorescence. Whole cell voltage and current clamp recordings were performed on DIV 22-29 cultures using an Axopatch 200B amplifier with a National Instruments NIDAQ-MX digital acquisition system and results acquired and analysed with WinEDR V3.9.1 software. Experiments were performed at 35-37ºC in atmospheric air using an extracellular solution containing the following ion concentrations (in mM) to mimic the potassium concentration of the cell culture media and concentration of other ions in cerebrospinal fluid 144 NaCl, 5.3 KCl, 2.5 $CaCl_2$, 1 $MgCl_2$, 1 NaH_2PO_4, 10 HEPES, 10 mM glucose, pH 7.4 (Agathou and Káradóttir, 2019). Temperature was controlled using a TC-324C automatic temperature controller (Warner Instruments). The pipette solution contained (in mM): 130 K-gluconate, 4 NaCl, 0.5 $CaCl_2$, 10 HEPES 0.5 EGTA, pH 7.2 with KOH. Osmolarity of the external solution was 312 mOsm and the internal solution was 270 mOsm, both adjusted with sucrose. Borosilicate glass pipettes were pulled to a resistance of 5-20 MΩ.

To record from neurons, electrodes were brought into contact with the cell membrane and gigaOhm seals formed by gentle suction supplied from a syringe and water filled U tube. Firm suction was then

used to break the membrane under the pipette to form a whole-cell recording. Recordings exhibiting a leak of more than 100 pA were rejected at this stage. Within 2 seconds of whole-cell access, the amplifier was switched to current clamp mode to enable instantaneous membrane potential to be estimated. Recordings were made for 2 minutes in current clamp mode to measure neuronal activity at baseline and after 5 minutes treatment with neuromodulators.

Action potential firing frequency was calculated using the frequency analysis function in WinEDR (Strathclyde electrophysiology software, http://spider.science.strath.ac.uk/sipbs/software_ses.htm). Data were presented as the number of action potentials per second (Hz). Action potentials were defined as regenerative, all-or-nothing changes in membrane potential that produced an overshoot beyond 0 mV.

Statistical Analysis

Data were analysed using GraphPad Prism Version 10, with significance set at $p \leq 0.05$. Statistical tests used are indicated in the relevant figure legends.

Acknowledgements

We are grateful to Professors Ueli Suter and Pierre Chambon, and Dr Daniel Metzger for gift of the PLP-Cre-ERT2 mice. Dr Katherine Kusch (Nave lab) and Professor Ori Peles kindly provided antibodies to MCT1 and Caspr1, respectively. EM processing and sectioning of conditional *Kif21*b and *Tubb4a* knockout mice was performed with assistance from Mrs Margaret Mullin in the Glasgow Imaging Facility; Dr Paul Montague provided genotyping. We are grateful to Dr Michaela Schweizer and Dr Mary Muhia (Hamburg) for assistance in respect to the conditional *Kif21b* knockout mice. J.M.E. and E.R.B. were supported by grants from the UK MS Society (Grants 58 to JME; Grant 127 to JME and ERB). J.M.E. was also supported by funds from the Chief Scientist's Office, Scotland and the University of Glasgow (SPRINT MND/MS PhD studentship) and the National Centre for the Replacement, Refinement and Reduction of Animals in Research (NC3Rs). K.A.N. was supported by the European Research Council (AdvGrant MyeliNANO), the Dr. Myriam and Sheldon Adelson Medical Foundation (AMRF) and the German Research Council (DFG-TRR274). SG was supported by the Deutsche Forschungsgemeinschaft GO 2463/1-1 to.

Authors' contributions
Conceptualization JME, KAN, SG, ERB.
Data curation, KC, JME.
Formal Analysis KC, SW, Y-H C, UG, MLA, YK, ERB, JME.
Funding acquisition, JME, KAN, SG, ERB.
Investigation KC, SW, UG, MLA, YK, LP-F, ERB, JME.
Methodology AB, TG, CLC, RSS, LK
Project administration JME, KAN, SG
Resources MK, CK, HBW
Supervision JME, SG, ERB
Visualization, JME, KC
Writing – original draft JME, KAN
Writing – review & editing SG, ERB, KC, MK, CC, HW All authors
All authors approved the manuscript

Bibliography

Agathou, S., and Káradóttir, R.T. (2019). Whole-Cell Patch Clamp Recordings from Oligodendrocyte Lineage Cells in Brain Slices. Methods Mol. Biol. *1936*, 141–168.
Aggarwal, S., Yurlova, L., Snaidero, N., Reetz, C., Frey, S., Zimmermann, J., Pähler, G., Janshoff, A., Friedrichs, J., Müller, D.J., et al. (2011). A size barrier limits protein diffusion at the cell surface to generate lipid-rich myelin-membrane sheets. Dev. Cell *21*, 445–456.
Ainger, K., Avossa, D., Morgan, F., Hill, S.J., Barry, C., Barbarese, E., and Carson, J.H. (1993). Transport and localization of exogenous myelin basic protein mRNA microinjected into oligodendrocytes. J. Cell Biol. *123*, 431–441.
Al-Abdi, L., Al Murshedi, F., Elmanzalawy, A., Al Habsi, A., Helaby, R., Ganesh, A., Ibrahim, N., Patel, N., and Alkuraya, F.S. (2020). CNP deficiency causes severe hypomyelinating leukodystrophy in humans. Hum. Genet. *139*, 615–622.
Allen, R.D., Metuzals, J., Tasaki, I., Brady, S.T., and Gilbert, S.P. (1982). Fast axonal transport in squid giant axon. Science *218*, 1127–1129.
Austin, L., Bray, J.J., and Young, R.J. (1966). Transport of proteins and ribonucleic acid along nerve axons. J. Neurochem. *13*, 1267–1269.
Balice-Gordon, R.J., Bone, L.J., and Scherer, S.S. (1998). Functional gap junctions in the schwann cell myelin sheath. J. Cell Biol. *142*, 1095–1104.
Baraban, M., Koudelka, S., and Lyons, D.A. (2018). Ca 2+ activity signatures of myelin sheath formation and growth in vivo. Nat. Neurosci. *21*, 19–23.
Barry, C., Pearson, C., and Barbarese, E. (1996). Morphological organization of oligodendrocyte processes during development in culture and in vivo. Dev Neurosci *18*, 233–242.
Bhat, M.A. (2003). Molecular organization of axo-glial junctions. Curr. Opin. Neurobiol. *13*, 552–559.
Blakemore, W.F. (1969). Schmidt-Lantermann incisures in the central nervous system. J Ultrastruct Res *29*, 496–498.
Borys, F., Joachimiak, E., Krawczyk, H., and Fabczak, H. (2020). Intrinsic and extrinsic factors affecting microtubule dynamics in normal and cancer cells. Molecules *25*.
Brady, S.T. (1985). A novel brain ATPase with properties expected for the fast axonal transport motor. Nature *317*, 73–75.
Brady, S.T., Lasek, R.J., and Allen, R.D. (1982). Fast axonal transport in extruded axoplasm from squid giant axon. Science *218*, 1129–1131.
Brockschnieder, D., Sabanay, H., Riethmacher, D., and Peles, E. (2006). Ermin, a myelinating oligodendrocyte-specific protein that regulates cell morphology. J. Neurosci. *26*, 757–762.
Brophy, P.J., Boccaccio, G.L., and Colman, D.R. (1993). The distribution of myelin basic protein mRNAs within myelinating oligodendrocytes. Trends Neurosci. *16*, 515–521.
Brown, T.L., and Macklin, W.B. (2020). The actin cytoskeleton in myelinating cells. Neurochem. Res. *45*, 684–693.
Burzynska, A.Z., Anderson, C., Arciniegas, D.B., Calhoun, V., Choi, I.-Y., Mendez Colmenares, A., Kramer, A.F., Li, K., Lee, J., Lee, P., et al. (2024). Correlates of axonal content in healthy adult span: Age, sex, myelin, and metabolic health. Cereb. Circ. Cogn. Behav. *6*, 100203.
Butt, A.M., and Ransom, B.R. (1989). Visualization of oligodendrocytes and astrocytes in the intact rat optic nerve by intracellular injection of lucifer yellow and horseradish peroxidase. Glia *2*, 470–475.
Carson, J.H., Worboys, K., Ainger, K., and Barbarese, E. (1997). Translocation of myelin basic protein mRNA in oligodendrocytes requires microtubules and kinesin. Cell Motil. Cytoskeleton *38*, 318–328.
Carson, J.H., Kwon, S., and Barbarese, E. (1998). RNA trafficking in myelinating cells. Curr. Opin. Neurobiol. *8*, 607–612.

Cason, S.E., and Holzbaur, E.L.F. (2022). Selective motor activation in organelle transport along axons. Nat. Rev. Mol. Cell Biol. *23*, 699–714.
Chamberlain, K.A., Huang, N., Xie, Y., LiCausi, F., Li, S., Li, Y., and Sheng, Z.-H. (2021). Oligodendrocytes enhance axonal energy metabolism by deacetylation of mitochondrial proteins through transcellular delivery of SIRT2. Neuron *109*, 3456–3472.e8.
Cohen, C.C.H., Popovic, M.A., Klooster, J., Weil, M.-T., Möbius, W., Nave, K.-A., and Kole, M.H.P. (2020). Saltatory Conduction along Myelinated Axons Involves a Periaxonal Nanocircuit. Cell *180*, 311–322.e15.
Colman, D.R., Kreibich, G., Frey, A.B., and Sabatini, D.D. (1982). Synthesis and incorporation of myelin polypeptides into CNS myelin. J. Cell Biol. *95*, 598–608.
Covill-Cooke, C., Toncheva, V.S., and Kittler, J.T. (2021). Regulation of peroxisomal trafficking and distribution. Cell Mol. Life Sci. *78*, 1929–1941.
Edgar, J.M., and Garbern, J. (2004). The myelinated axon is dependent on the myelinating cell for support and maintenance: molecules involved. J. Neurosci. Res. *76*, 593–598.
Edgar, J.M., and Griffiths, I.R. (2013). White matter structure: a microscopist's view. In Diffusion MRI , H. Johansen-Berg, and T.E.J. Behrens, eds. (London: Elsevier), pp. 127–149.
Edgar, J.M., McLaughlin, M., Yool, D., Zhang, S.-C., Fowler, J.H., Montague, P., Barrie, J.A., McCulloch, M.C., Duncan, I.D., Garbern, J., et al. (2004). Oligodendroglial modulation of fast axonal transport in a mouse model of hereditary spastic paraplegia. J. Cell Biol. *166*, 121–131.
Edgar, J.M., McLaughlin, M., Werner, H.B., McCulloch, M.C., Barrie, J.A., Brown, A., Faichney, A.B., Snaidero, N., Nave, K.-A., and Griffiths, I.R. (2009). Early ultrastructural defects of axons and axon-glia junctions in mice lacking expression of Cnp1. Glia *57*, 1815–1824.
Edgar, J.M., Smith, R.S., and Duncan, I.D. (2020). Transmission electron microscopy and morphometry of the CNS white matter. Methods Mol. Biol. *2143*, 233–261.
Edgar, J.M., McGowan, E., Chapple, K.J., Möbius, W., Lemgruber, L., Insall, R.H., Nave, K.-A., and Boullerne, A. (2021). Río-Hortega's drawings revisited with fluorescent protein defines a cytoplasm-filled channel system of CNS myelin. J. Anat. *239*, 1241–1255.
Erwig, M.S., Hesse, D., Jung, R.B., Uecker, M., Kusch, K., Tenzer, S., Jahn, O., and Werner, H.B. (2019). Myelin: methods for purification and proteome analysis. Methods Mol. Biol. *1936*, 37–63.
Farley, F.W., Soriano, P., Steffen, L.S., and Dymecki, S.M. (2000). Widespread recombinase expression using FLPeR (flipper) mice. Genesis *28*, 106–110.
Frühbeis, C., Kuo-Elsner, W.P., Müller, C., Barth, K., Peris, L., Tenzer, S., Möbius, W., Werner, H.B., Nave, K.-A., Fröhlich, D., et al. (2020). Oligodendrocytes support axonal transport and maintenance via exosome secretion. PLoS Biol. *18*, e3000621.
Fu, M.-M., McAlear, T.S., Nguyen, H., Oses-Prieto, J.A., Valenzuela, A., Shi, R.D., Perrino, J.J., Huang, T.-T., Burlingame, A.L., Bechstedt, S., et al. (2019). The golgi outpost protein TPPP nucleates microtubules and is critical for myelination. Cell *179*, 132–146.e14.
Fünfschilling, U., Supplie, L.M., Mahad, D., Boretius, S., Saab, A.S., Edgar, J., Brinkmann, B.G., Kassmann, C.M., Tzvetanova, I.D., Möbius, W., et al. (2012). Glycolytic oligodendrocytes maintain myelin and long-term axonal integrity. Nature *485*, 517–521.
García-Mateo, N., Pascua-Maestro, R., Pérez-Castellanos, A., Lillo, C., Sanchez, D., and Ganfornina, M.D. (2018). Myelin extracellular leaflet compaction requires apolipoprotein D membrane management to optimize lysosomal-dependent recycling and glycocalyx removal. Glia *66*, 670–687.
Gargareta, V.-I., Reuschenbach, J., Siems, S.B., Sun, T., Piepkorn, L., Mangana, C., Späte, E., Goebbels, S., Huitinga, I., Möbius, W., et al. (2022). Conservation and divergence of myelin proteome and oligodendrocyte transcriptome profiles between humans and mice. Elife *11*.
Genoud, S., Lappe-Siefke, C., Goebbels, S., Radtke, F., Aguet, M., Scherer, S.S., Suter, U., Nave, K.-A., and Mantei, N. (2002). Notch1 control of oligodendrocyte differentiation in the spinal cord. J. Cell Biol. *158*, 709–718.

Ghiretti, A.E., Thies, E., Tokito, M.K., Lin, T., Ostap, E.M., Kneussel, M., and Holzbaur, E.L.F. (2016). Activity-Dependent Regulation of Distinct Transport and Cytoskeletal Remodeling Functions of the Dendritic Kinesin KIF21B. Neuron *92*, 857–872.
Goris, A., Boonen, S., D'hooghe, M.B., and Dubois, B. (2010). Replication of KIF21B as a susceptibility locus for multiple sclerosis. J. Med. Genet. *47*, 775–776.
Grafstein, B. (1967). Transport of protein by goldfish optic nerve fibers. Science *157*, 196–198.
Hagemeyer, N., Goebbels, S., Papiol, S., Kästner, A., Hofer, S., Begemann, M., Gerwig, U.C., Boretius, S., Wieser, G.L., Ronnenberg, A., et al. (2012). A myelin gene causative of a catatonia-depression syndrome upon aging. EMBO Mol. Med. *4*, 528–539.
Harauz, G., Ladizhansky, V., and Boggs, J.M. (2009). Structural polymorphism and multifunctionality of myelin basic protein. Biochemistry *48*, 8094–8104.
Hartline, D.K., and Colman, D.R. (2007). Rapid conduction and the evolution of giant axons and myelinated fibers. Curr. Biol. *17*, R29-35.
Hirano, A., and Dembitzer, H.M. (1967). A structural analysis of the myelin sheath in the central nervous system. J. Cell Biol. *34*, 555–567.
Holz, A., Schaeren-Wiemers, N., Schaefer, C., Pott, U., Colello, R.J., and Schwab, M.E. (1996). Molecular and developmental characterization of novel cDNAs of the myelin-associated/oligodendrocytic basic protein. J. Neurosci. *16*, 467–477.
Hooikaas, P.J., Damstra, H.G., Gros, O.J., van Riel, W.E., Martin, M., Smits, Y.T., van Loosdregt, J., Kapitein, L.C., Berger, F., and Akhmanova, A. (2020). Kinesin-4 KIF21B limits microtubule growth to allow rapid centrosome polarization in T cells. Elife *9*.
Iyer, M., Kantarci, H., Cooper, M.H., Ambiel, N., Novak, S.W., Andrade, L.R., Lam, M., Jones, G., Münch, A.E., Yu, X., et al. (2024). Oligodendrocyte calcium signaling promotes actin-dependent myelin sheath extension. Nat. Commun. *15*, 265.
Jahn, O., Siems, S.B., Kusch, K., Hesse, D., Jung, R.B., Liepold, T., Uecker, M., Sun, T., and Werner, H.B. (2020). The CNS Myelin Proteome: Deep Profile and Persistence After Post-mortem Delay. Front. Cell Neurosci. *14*, 239.
Janke, C., and Bulinski, J.C. (2011). Post-translational regulation of the microtubule cytoskeleton: mechanisms and functions. Nat. Rev. Mol. Cell Biol. *12*, 773–786.
Jansen, K.I., Iwanski, M.K., Burute, M., and Kapitein, L.C. (2023). A live-cell marker to visualize the dynamics of stable microtubules throughout the cell cycle. J. Cell Biol. *222*.
Kachar, B., Behar, T., and Dubois-Dalcq, M. (1986). Cell shape and motility of oligodendrocytes cultured without neurons. Cell Tissue Res. *244*, 27–38.
Kassmann, C.M., Lappe-Siefke, C., Baes, M., Brügger, B., Mildner, A., Werner, H.B., Natt, O., Michaelis, T., Prinz, M., Frahm, J., et al. (2007). Axonal loss and neuroinflammation caused by peroxisome-deficient oligodendrocytes. Nat. Genet. *39*, 969–976.
Kesarwani, S., Lama, P., Chandra, A., Reddy, P.P., Jijumon, A.S., Bodakuntla, S., Rao, B.M., Janke, C., Das, R., and Sirajuddin, M. (2020). Genetically encoded live-cell sensor for tyrosinated microtubules. J. Cell Biol. *219*.
Krasnow, A.M., Ford, M.C., Valdivia, L.E., Wilson, S.W., and Attwell, D. (2018). Regulation of developing myelin sheath elongation by oligodendrocyte calcium transients in vivo. Nat. Neurosci. *21*, 24–28.
Kreft, K.L., van Meurs, M., Wierenga-Wolf, A.F., Melief, M.-J., van Strien, M.E., Hol, E.M., Oostra, B.A., Laman, J.D., and Hintzen, R.Q. (2014). Abundant kif21b is associated with accelerated progression in neurodegenerative diseases. Acta Neuropathol. Commun. *2*, 144.
Kursula, P., Lehto, V.P., and Heape, A.M. (2001). The small myelin-associated glycoprotein binds to tubulin and microtubules. Brain Res. Mol. Brain Res. *87*, 22–30.
Kusch, K., Uecker, M., Liepold, T., Möbius, W., Hoffmann, C., Neumann, H., Werner, H.B., and Jahn, O. (2017). Partial Immunoblotting of 2D-Gels: A Novel Method to Identify Post-Translationally Modified Proteins Exemplified for the Myelin Acetylome. Proteomes *5*.

Labonté, D., Thies, E., and Kneussel, M. (2014). The kinesin KIF21B participates in the cell surface delivery of γ2 subunit-containing GABAA receptors. Eur. J. Cell Biol. *93*, 338–346.
Lappe-Siefke, C., Goebbels, S., Gravel, M., Nicksch, E., Lee, J., Braun, P.E., Griffiths, I.R., and Nave, K.-A. (2003). Disruption of Cnp1 uncouples oligodendroglial functions in axonal support and myelination. Nat. Genet. *33*, 366–374.
Lasek, R.J. (1967). Bidirectional transport of radioactively labelled axoplasmic components. Nature *216*, 1212–1214.
Lee, Y., Morrison, B.M., Li, Y., Lengacher, S., Farah, M.H., Hoffman, P.N., Liu, Y., Tsingalia, A., Jin, L., Zhang, P.-W., et al. (2012). Oligodendroglia metabolically support axons and contribute to neurodegeneration. Nature *487*, 443–448.
Lehotzky, A., Lau, P., Tokési, N., Muja, N., Hudson, L.D., and Ovádi, J. (2010). Tubulin polymerization-promoting protein (TPPP/p25) is critical for oligodendrocyte differentiation. Glia *58*, 157–168.
Leone, D.P., Genoud, S., Atanasoski, S., Grausenburger, R., Berger, P., Metzger, D., Macklin, W.B., Chambon, P., and Suter, U. (2003). Tamoxifen-inducible glia-specific Cre mice for somatic mutagenesis in oligodendrocytes and Schwann cells. Mol. Cell. Neurosci. *22*, 430–440.
Livett, B.G., Geffen, L.B., and Austin, L. (1968). Axoplasmic transport of 14C-noradrenaline and protein in splenic nerves. Nature *217*, 278–279.
Looser, Z.J., Ravotto, L., Jung, R.B., Werner, H.B., Ruhwedel, T., Möbius, W., Bergles, D.E., Barros, L.F., Nave, K.-A., Weber, B., et al. (2022). Potassium regulates axon-oligodendrocyte signaling and metabolic coupling in white matter. BioRxiv.
Looser, Z.J., Faik, Z., Ravotto, L., Zanker, H.S., Jung, R.B., Werner, H.B., Ruhwedel, T., Möbius, W., Bergles, D.E., Barros, L.F., et al. (2024). Oligodendrocyte-axon metabolic coupling is mediated by extracellular K+ and maintains axonal health. Nat. Neurosci. *27*, 433–448.
Lubinska, L. (1964). Axoplasmic streaming in regenerating and in normal nerve fibres. Prog. Brain Res. *13*, 1–71.
Lunn, K.F., Clayton, M.K., and Duncan, I.D. (1997). The temporal progression of the myelination defect in the taiep rat. J Neurocytol *26*, 267–281.
Madisen, L., Zwingman, T.A., Sunkin, S.M., Oh, S.W., Zariwala, H.A., Gu, H., Ng, L.L., Palmiter, R.D., Hawrylycz, M.J., Jones, A.R., et al. (2010). A robust and high-throughput Cre reporting and characterization system for the whole mouse brain. Nat. Neurosci. *13*, 133–140.
Marner, L., Nyengaard, J.R., Tang, Y., and Pakkenberg, B. (2003). Marked loss of myelinated nerve fibers in the human brain with age. J. Comp. Neurol. *462*, 144–152.
Marszalek, J.R., Weiner, J.A., Farlow, S.J., Chun, J., and Goldstein, L.S. (1999). Novel dendritic kinesin sorting identified by different process targeting of two related kinesins: KIF21A and KIF21B. J. Cell Biol. *145*, 469–479.
Meschkat, M., Steyer, A.M., Weil, M.-T., Kusch, K., Jahn, O., Piepkorn, L., Agüi-Gonzalez, P., Ngoc Phan, N.T., Ruhwedel, T., Sadowski, B., et al. (2020). White matter integrity requires continuous myelin synthesis at the inner tongue. BioRxiv.
Micu, I., Plemel, J.R., Lachance, C., Proft, J., Jansen, A.J., Cummins, K., van Minnen, J., and Stys, P.K. (2016). The molecular physiology of the axo-myelinic synapse. Exp. Neurol. *276*, 41–50.
Micu, I., Plemel, J.R., Caprariello, A.V., Nave, K.-A., and Stys, P.K. (2018). Axo-myelinic neurotransmission: a novel mode of cell signalling in the central nervous system. Nat. Rev. Neurosci. *19*, 49–58.
Möbius, W., Nave, K.-A., and Werner, H.B. (2016). Electron microscopy of myelin: Structure preservation by high-pressure freezing. Brain Res. *1641*, 92–100.
Mueller, S.G. (2024). 7T MP2RAGE for cortical myelin segmentation: Impact of aging. PLoS One *19*, e0299670.
Muhia, M., Thies, E., Labonté, D., Ghiretti, A.E., Gromova, K.V., Xompero, F., Lappe-Siefke, C., Hermans-Borgmeyer, I., Kuhl, D., Schweizer, M., et al. (2016). The kinesin KIF21B regulates

microtubule dynamics and is essential for neuronal morphology, synapse function, and learning and memory. Cell Rep. *15*, 968–977.
Mukherjee, C., Kling, T., Russo, B., Miebach, K., Kess, E., Schifferer, M., Pedro, L.D., Weikert, U., Fard, M.K., Kannaiyan, N., et al. (2020). Oligodendrocytes provide antioxidant defense function for neurons by secreting ferritin heavy chain. Cell Metab. *32*, 259–272.e10.
Nakamura, D.S., Lin, Y.H., Khan, D., Gothié, J.-D.M., de Faria, O., Dixon, J.A., McBride, H.M., Antel, J.P., and Kennedy, T.E. (2021). Mitochondrial dynamics and bioenergetics regulated by netrin-1 in oligodendrocytes. Glia *69*, 392–412.
Nave, K.-A. (2010a). Myelination and the trophic support of long axons. Nat. Rev. Neurosci. *11*, 275–283.
Nave, K.-A. (2010b). Myelination and support of axonal integrity by glia. Nature *468*, 244–252.
Nawaz, S., Sánchez, P., Schmitt, S., Snaidero, N., Mitkovski, M., Velte, C., Brückner, B.R., Alexopoulos, I., Czopka, T., Jung, S.Y., et al. (2015). Actin filament turnover drives leading edge growth during myelin sheath formation in the central nervous system. Dev. Cell *34*, 139–151.
Ochs, S., Johnson, J., and Ng, M.H. (1967). Protein incorporation and axoplasmic flow in motoneuron fibres following intra-cord injection of labelled leucine. J. Neurochem. *14*, 317–331.
O'Connor, L.T., Goetz, B.D., Couve, E., Song, J., and Duncan, I.D. (2000). Intracellular distribution of myelin protein gene products is altered in oligodendrocytes of the taiep rat. Mol. Cell. Neurosci. *16*, 396–407.
Perge, J.A., Niven, J.E., Mugnaini, E., Balasubramanian, V., and Sterling, P. (2012). Why do axons differ in caliber? J. Neurosci. *32*, 626–638.
Peters, A. (1960). The formation and structure of myelin sheaths in the central nervous system. J Biophys Biochem Cytol *8*, 431–446.
Peters, A. (2002). The effects of normal aging on myelin and nerve fibers: a review. J Neurocytol *31*, 581–593.
Peters, A., and Kemper, T. (2012). A review of the structural alterations in the cerebral hemispheres of the aging rhesus monkey. Neurobiol. Aging *33*, 2357–2372.
Quraishe, S., Wyttenbach, A., Matinyarare, N., Perry, V.H., Fern, R., and O'Connor, V. (2016). Selective and compartmentalized myelin expression of HspB5. Neuroscience *316*, 130–142.
Rapp, S., Saffrich, R., Anton, M., Jäkle, U., Ansorge, W., Gorgas, K., and Just, W.W. (1996). Microtubule-based peroxisome movement. J. Cell Sci. *109 (Pt 4)*, 837–849.
Renthal, R., Schneider, B.G., Miller, M.M., and Ludueña, R.F. (1993). Beta IV is the major beta-tubulin isotype in bovine cilia. Cell Motil. Cytoskeleton *25*, 19–29.
Richert, S., Kleinecke, S., Günther, J., Schaumburg, F., Edgar, J., Nienhaus, G.U., Nave, K.-A., and Kassmann, C.M. (2014). In vivo labeling of peroxisomes by photoconvertible mEos2 in myelinating glia of mice. Biochimie *98*, 127–134.
van Riel, W.E., Rai, A., Bianchi, S., Katrukha, E.A., Liu, Q., Heck, A.J., Hoogenraad, C.C., Steinmetz, M.O., Kapitein, L.C., and Akhmanova, A. (2017). Kinesin-4 KIF21B is a potent microtubule pausing factor. Elife *6*.
Saab, A.S., and Nave, K.-A. (2017). Myelin dynamics: protecting and shaping neuronal functions. Curr. Opin. Neurobiol. *47*, 104–112.
Saab, A.S., Tzvetanova, I.D., and Nave, K.-A. (2013). The role of myelin and oligodendrocytes in axonal energy metabolism. Curr. Opin. Neurobiol. *23*, 1065–1072.
Saab, A.S., Tzvetavona, I.D., Trevisiol, A., Baltan, S., Dibaj, P., Kusch, K., Möbius, W., Goetze, B., Jahn, H.M., Huang, W., et al. (2016). Oligodendroglial NMDA receptors regulate glucose import and axonal energy metabolism. Neuron *91*, 119–132.
Schaeren-Wiemers, N., Schaefer, C., Valenzuela, D.M., Yancopoulos, G.D., and Schwab, M.E. (1995). Identification of new oligodendrocyte- and myelin-specific genes by a differential screening approach. J. Neurochem. *65*, 10–22.
Schäffner, E., Bosch-Queralt, M., Edgar, J.M., Lehning, M., Strauß, J., Fleischer, N., Kungl, T.,

Wieghofer, P., Berghoff, S.A., Reinert, T., et al. (2023). Myelin insulation as a risk factor for axonal degeneration in autoimmune demyelinating disease. Nat. Neurosci. *26*, 1218–1228.
Schindelin, J., Arganda-Carreras, I., Frise, E., Kaynig, V., Longair, M., Pietzsch, T., Preibisch, S., Rueden, C., Saalfeld, S., Schmid, B., et al. (2012). Fiji: an open-source platform for biological-image analysis. Nat. Methods *9*, 676–682.
Snaidero, N., Möbius, W., Czopka, T., Hekking, L.H.P., Mathisen, C., Verkleij, D., Goebbels, S., Edgar, J., Merkler, D., Lyons, D.A., et al. (2014). Myelin membrane wrapping of CNS axons by PI(3,4,5)P3-dependent polarized growth at the inner tongue. Cell *156*, 277–290.
Snaidero, N., Velte, C., Myllykoski, M., Raasakka, A., Ignatev, A., Werner, H.B., Erwig, M.S., Möbius, W., Kursula, P., Nave, K.-A., et al. (2017). Antagonistic functions of MBP and CNP establish cytosolic channels in CNS myelin. Cell Rep. *18*, 314–323.
Song, J., O'connor, L.T., Yu, W., Baas, P.W., and Duncan, I.D. (1999). Microtubule alterations in cultured taiep rat oligodendrocytes lead to deficits in myelin membrane formation. J Neurocytol *28*, 671–683.
Song, J., Carson, J.H., Barbarese, E., Li, F.-Y., and Duncan, I.D. (2003). RNA transport in oligodendrocytes from the taiep mutant rat. Mol. Cell. Neurosci. *24*, 926–938.
Späte, E., Zhou, B., Sun, T., Kusch, K., Asadollahi, E., Siems, S.B., Depp, C., Werner, H.B., Saher, G., Hirrlinger, J., et al. (2024). Downregulated expression of lactate dehydrogenase in adult oligodendrocytes and its implication for the transfer of glycolysis products to axons. Glia.
Spencer, P.S., and Thomas, P.K. (1974). Ultrastructural studies of the dying-back process. II. The sequestration and removal by Schwann cells and oligodendrocytes of organelles from normal and diseases axons. J Neurocytol *3*, 763–783.
Stassart, R.M., Möbius, W., Nave, K.-A., and Edgar, J.M. (2018). The Axon-Myelin Unit in Development and Degenerative Disease. Front. Neurosci. *12*, 467.
Sternberger, N.H., Itoyama, Y., Kies, M.W., and Webster H deF (1978). Immunocytochemical method to identify basic protein in myelin-forming oligodendrocytes of newborn rat C.N.S. J Neurocytol *7*, 251–263.
Steyer, A.M., Buscham, T.J., Lorenz, C., Hümmert, S., Eichel-Vogel, M.A., Schadt, L.C., Edgar, J.M., Köster, S., Möbius, W., Nave, K.-A., et al. (2023). Focused ion beam-scanning electron microscopy links pathological myelin outfoldings to axonal changes in mice lacking Plp1 or Mag. Glia *71*, 509–523.
Stys, P.K. (2011). The axo-myelinic synapse. Trends Neurosci. *34*, 393–400.
Stys, P.K., Ransom, B.R., and Waxman, S.G. (1991). Compound action potential of nerve recorded by suction electrode: a theoretical and experimental analysis. Brain Res. *546*, 18–32.
Tang, Y., Nyengaard, J.R., Pakkenberg, B., and Gundersen, H.J. (1997). Age-induced white matter changes in the human brain: a stereological investigation. Neurobiol. Aging *18*, 609–615.
Taylor, K.R., and Monje, M. (2023). Neuron-oligodendroglial interactions in health and malignant disease. Nat. Rev. Neurosci. *24*, 733–746.
Terada, N., Kidd, G.J., Kinter, M., Bjartmar, C., Moran-Jones, K., and Trapp, B.D. (2005). Beta IV tubulin is selectively expressed by oligodendrocytes in the central nervous system. Glia *50*, 212–222.
Thomson, C.E., McCulloch, M., Sorenson, A., Barnett, S.C., Seed, B.V., Griffiths, I.R., and McLaughlin, M. (2008). Myelinated, synapsing cultures of murine spinal cord--validation as an in vitro model of the central nervous system. Eur. J. Neurosci. *28*, 1518–1535.
Tokési, N., Lehotzky, A., Horváth, I., Szabó, B., Oláh, J., Lau, P., and Ovádi, J. (2010). TPPP/p25 promotes tubulin acetylation by inhibiting histone deacetylase 6. J. Biol. Chem. *285*, 17896–17906.
Trapp, B.D., Moench, T., Pulley, M., Barbosa, E., Tennekoon, G., and Griffin, J. (1987). Spatial segregation of mRNA encoding myelin-specific proteins. Proc. Natl. Acad. Sci. USA *84*, 7773–7777.
Trapp, B.D., Bernier, L., Andrews, S.B., and Colman, D.R. (1988). Cellular and subcellular

distribution of 2’,3’-cyclic nucleotide 3’-phosphodiesterase and its mRNA in the rat central nervous system. J. Neurochem. *51*, 859–868.
Vale, R.D., Schnapp, B.J., Reese, T.S., and Sheetz, M.P. (1985). Movement of organelles along filaments dissociated from the axoplasm of the squid giant axon. Cell *40*, 449–454.
Vargas, J.N.S., Sleigh, J.N., and Schiavo, G. (2022). Coupling axonal mRNA transport and local translation to organelle maintenance and function. Curr. Opin. Cell Biol. *74*, 97–103.
Velumian, A.A., Samoilova, M., and Fehlings, M.G. (2011). Visualization of cytoplasmic diffusion within living myelin sheaths of CNS white matter axons using microinjection of the fluorescent dye Lucifer Yellow. Neuroimage *56*, 27–34.
Weber, P., Metzger, D., and Chambon, P. (2001). Temporally controlled targeted somatic mutagenesis in the mouse brain. Eur. J. Neurosci. *14*, 1777–1783.
Weiss, P., and Holland, Y. (1967). Neuronal dynamics and axonal flow, ii. The olfactory nerve as model test object. Proc. Natl. Acad. Sci. USA *57*, 258–264.
Werner, H.B., Kuhlmann, K., Shen, S., Uecker, M., Schardt, A., Dimova, K., Orfaniotou, F., Dhaunchak, A., Brinkmann, B.G., Möbius, W., et al. (2007). Proteolipid protein is required for transport of sirtuin 2 into CNS myelin. J. Neurosci. *27*, 7717–7730.
Weruaga-Prieto, E., Eggli, P., and Celio, M.R. (1996). Topographic variations in rat brain oligodendrocyte morphology elucidated by injection of Lucifer Yellow in fixed tissue slices. J Neurocytol *25*, 19–31.
Yamazaki, Y., Hozumi, Y., Kaneko, K., Fujii, S., Goto, K., and Kato, H. (2010). Oligodendrocytes: facilitating axonal conduction by more than myelination. Neuroscientist *16*, 11–18.
Young, K.M., Psachoulia, K., Tripathi, R.B., Dunn, S.-J., Cossell, L., Attwell, D., Tohyama, K., and Richardson, W.D. (2013). Oligodendrocyte dynamics in the healthy adult CNS: evidence for myelin remodeling. Neuron *77*, 873–885.
Zahavi, E.E., and Hoogenraad, C.C. (2021). Multiple layers of spatial regulation coordinate axonal cargo transport. Curr. Opin. Neurobiol. *69*, 241–246.
Zheng, C., Herve, B., Meijer, M., Rubio Rodriguez-Kirby, L.A., Guerreiro Cacais, A.O., Kukanja, P., Kabbe, M., Olsson, T., Agirre, E., and Castelo-Branco, G. (2023). Distinct transcriptomic and epigenomic responses of mature oligodendrocytes during disease progression in a mouse model of multiple sclerosis. BioRxiv.
Zuchero, J.B., Fu, M.-M., Sloan, S.A., Ibrahim, A., Olson, A., Zaremba, A., Dugas, J.C., Wienbar, S., Caprariello, A.V., Kantor, C., et al. (2015). CNS myelin wrapping is driven by actin disassembly. Dev. Cell *34*, 152–167.